Optimal Design of a Coupled Photovoltaic-Electrolysis-Battery System for Hydrogen Generation

Journal:	*Sustainable Energy & Fuels*
Manuscript ID	SE-ART-11-2022-001555.R1
Article Type:	Paper
Date Submitted by the Author:	01-Feb-2023
Complete List of Authors:	Alobaid, Aisha; Kuwait University College of Engineering and Petroleum, Chemical Engineering Adomaitis, Raymond; University of Maryland at College Park, Chemical Engineering

Optimal Design of a Coupled Photovoltaic-Electrolysis-Battery System for Hydrogen Generation

Aisha Alobaid*[a,b] and Raymond A. Adomaitis[a]

[a] *Department of Chemical and Biomolecular Engineering, Institute for Systems Research, University of Maryland, College Park, MD, 20742, USA*

[b] *Chemical Engineering Department, College of Engineering and Petroleum, Kuwait University, 13060, Kuwait*

Abstract

A computational algorithm to model an integrated photovoltaic-electrolysis-battery system is presented with the goal of identifying the system's optimal size, from a Pareto Front analysis perspective, that maximizes the hydrogen production rate, minimizes the levelized cost of energy (LCE) and total system's cost, while targeting a net-zero grid energy operation. Over 2 million sizing combinations were evaluated, 10 were chosen as the Pareto Front for this optimization problem, with hydrogen production capacities between 36-122 Nm^3/h and LCE values close to 0.2 \$/kWh. The results demonstrated that optimizing the system's cost and hydrogen production rate implicitly ensures LCE is minimized. The identified Pareto Front serves as a design guide, enabling the design of arbitrary plant capacities by multiplying a Pareto optimal point by a factor, while guaranteeing the new point still lies within the Pareto Front. This computational platform to model integrated solar-hydrogen systems can be extended to more complex hybrid systems.

Keywords: Green hydrogen, Optimization, Electrolysis, Solar, Hydrogen production.

---

*Corresponding author
Email: aisha.alobaid@ku.edu.kw
Address: Chemical Engineering Department, College of Engineering and Petroleum, Kuwait University, P.O.Box 5969, Safat, 13060, Kuwait

Nomenclature

ACS	Annual cost of the system (\$/yr)
AM	Air mass
ast	Apparent solar time
Cap	Battery capacity (kWh)
$C_{a,j}$	Annual cost of component j (\$/yr)
C_{aCapital}	Annualized capital cost (\$/yr)
$C_{\mathrm{aO\&M}}$	Annualized operation and maintenance cost (\$/yr)
C_{aRep}	Annualized replacement cost (\$/yr)
CRE	Capital recovery factor
DoD	Battery depth of discharge (%)
E_{an}	Annual energy produced by the PV system (kWh/yr)
E_b	Battery energy (kWh)
$GEIF$	The grid energy interaction factor
G_{cloudy}	Solar irradiance of a cloudy day (W/m^2)
G_D	Direct component of solar irradiance (W/m^2)
G_F	Diffuse component of solar irradiance (W/m^2)
G_G	Global irradiance (W/m^2)
G_{sc}	Solar constant (=1366 W/m^2)
G_{total}	Total solar irradiance (W/m^2)
I_o	Dark saturation current (A)
I_{ph}	Photo-current (A)
i	Real discount rate
LCE	Levelized cost of energy (\$/kWh)
M	Number of electrolysis stacks connected in parallel
M_{pv}	Number of PV modules connected in parallel
N	Number of cells connected in series

NGE	Net grid energy (kWh)
n_{H_2}	Hydrogen production rate (mol/s)
n_j	Lifetime of the j^{th} component (PV module, electrolyzer, battery) (yr)
$\vec{n_i}$	Vector normal to and pointing out of the PV module surface
P_e	Power of the Electrolyzer (kW)
P_{mp}	Maximum power point of the PV module (kW)
R_s	Series resistance (when used in diode equation) (Ω)
R_sh	Shunt resistance (Ω)
$RNGE$	Relative net grid energy (%)
$\vec{s}$	Solar radiation vector
SLF	The satisfied load fraction
STH	The solar to hydrogen conversion efficiency (%)
t_d	Number of days past the most recent winter solstice
UF	The utilization factor
U_j	Unit capital cost (\$/kW)
$U_{\mathrm{O\&M},j}$	Unit operating and maintenance cost (\$/kW)
V_{H_2}	Hydrogen volumetric production rate (Nm^3/h)
V_{mp}	Maximum power voltage (V)
V_{oc}	Open-circuit voltage (V)
X	Dimensionless concentration factor
z	Site elevation (km)
β	Diode ideality factor
δ	Earth's declination at $t_d = 0$ ($= 23.44^o$)
ζ	Zenith angle (^{o})
η	Overpotential (V)
η_{con}	Converter efficiency to/from utility grid (%)
η_b	Battery round-trip efficiency (%)

θ	Longitude (^{o})
θ_{tilt}	PV module tilt angle (^{o})
λ_y	Angle representing Earth's mean orbit (^{o})
ϕ	Latitude measured north of the equator (^{o})

1 Introduction

Currently, finite fossil fuel resources supply the vast majority of the world's energy demand [1]. The scarcity of fossil fuel resources, the rising global energy demand, and the measurable climate change have stressed the need for renewable energy sources [1].

Hydrogen, as an energy carrier, is a promising candidate to supply the world's energy demand. Nevertheless, significant technological barriers must be overcome for hydrogen to be competitive with current energy resources [2]. Research interest is growing in hydrogen-economy based applications through either enhancing current technologies or designing new production processes, enabling the production of hydrogen in an efficient and cost-effective manner. In addition to production, challenges in hydrogen storage, transportation, and distribution must be tackled simultaneously before the hydrogen economy can function at grid-scale level applications [3].

Currently, up to 96% of hydrogen production is fossil fuel based, which poses significant long-term environmental threats [4]. The hydrogen produced in such methods is referred to as grey hydrogen [5]. When the greenhouse gas emissions are captured or mitigated in the production process, then the produced hydrogen is classified as blue [5]. Green hydrogen is when renewable energy sources are utilized in the process, with no to minimum carbon emissions levels [5, 6].

Hydrogen production by water electrolysis is widely accepted to be the most sustainable source of green hydrogen production, especially when integrated with renewable energy sources such as solar or wind energy [4]. It also has the advantage that it is capable of producing extremely pure hydrogen (>99.999%), which is ideal for some applications such as fuel cell vehicles [7]. Despite it being known for over 200 years, hydrogen production from water electrolysis constitutes less than 4% of the current hydrogen economy [8].

Research efforts are still underway to optimize the design and operation of sustainable hydrogen production systems. Gibson and Kelly [9] investigated a coupled PV-electrolysis system, in which they examined different system designs to reach optimal solar to hydrogen (STH) efficiency.

They tested multiple commercial PV modules and concluded that directly coupling the two systems leads to optimal efficiency of 12.4% if the PV modules are specifically designed to have a maximum power voltage (V_{mp}) that matches the electrolyzer operating voltage. In other cases where there is a mismatch between the PV modules output voltage and the electrolyzer operating voltage, incorporating a DC-DC converter in the circuit is beneficial to reach acceptable STH values between 5.7 and 10.5% [9, 10]. Similar results were also highlighted by the work of Cabezas et al. [11]. They demonstrated that for a directly coupled PV-electrolyzer system, optimal design configurations correspond to cases where the PV modules maximum power point (MPP) matches the electrolyzer operating voltage. They also demonstrated that using state-of-art electrolyzers coupled with suitable design of PV modules can increase the system's coupling efficiency. Sriramagiri et al. [12] examined different coupling strategies for photovoltaic electrolyzer (PV-EC) systems to evaluate the solar-to-fuel efficiency (SFE) under actual operating conditions. They developed a model to evaluate the annual performance and applied it on two systems: a bench-scale PV-CO_2 EC and a MW-scale commercial PV-H_2O EC. The calculated SFE values under real-life operating conditions were up to 32% lower relative to standard testing conditions, with enhanced performance observed with the use of DC power optimizer compared to optimally matched and slightly mismatched directly coupled systems.

A hybrid system consisting of PV modules and wind turbines (WT) to power an electrolyzer is simulated in Khalilnejad et al. [13]. Achieving optimal design of WT and PV systems to maximize hydrogen production, while minimizing excess energy generated was the primary focus. The simulation was intended to support the operation of an off-grid electrolyzer load for a diurnal period (24 h simulation time) in Miami city.

Aside from the promising usage of hydrogen in fuel cells for transportation applications, hydrogen can serve as a solar energy storage medium in stand-alone systems, providing backup power in cases of diurnal weather and long-term seasonal variations [14]. Lagorse et al. [15] proposed a stand-alone street lighting hybrid system consisting of PV cells, storage battery, and hydrogen-powered fuel cells. The integration of fuel cells is essential in cases where the battery is unable to provide necessary power due to long-term seasonal variations. For Geneva, Switzerland, the optimal system sizing chosen to minimize the system cost, was able to power the street light all year round.

Hassan et al. [16] also investigated a similar hybrid energy system for grid-connected residential applications. The system consists of PV modules as the primary source of energy, coupled with a storage battery bank and a hydrogen storage system (electrolyzer, fuel cell, and hydrogen storage tanks) to cover dynamic load scenarios. They proposed different operation modes of the system based on the charging/discharging states of the battery and hydrogen storage systems. The hybrid system was able to meet the dynamic load demands with excellent grid stability over 24 h period in a typical summer day in Islamabad.

A techno-economic analysis of a grid connected hybrid energy system was presented in Singh et al. [17]. The hybrid system consists of PV modules, fuel cell stack, electrolyzer, and hydrogen storage tank, and is designed to meet the electrical load demands of a small community center in India. A power management strategy was proposed to maximize the system's efficiency and reliability. The results demonstrated that the grid-connected hybrid system was able to provide uninterrupted power supply and completely cover the energy demand of the community, with an optimal LCE value of 0.104 $/kWh.

Rullo et al. [18] presented an energy management strategy (EMS) that uses finite state machine approach to control a stand-alone hybrid system. The system consists of PV modules, wind turbines, battery bank, bioethanol reformer for hydrogen production, and a fuel cell system, and is intended to cover a dynamic load demand of a standard residential building. The management strategy was simulated and experimentally validated in a laboratory-scale station, and was able to maximum autonomy time, which corresponds to the battery ability to cover full load demands before reaching the minimum state of charge (SOC) level. The EMS was also able to accomplish minimal recharge time, with minimal cycles of charging and discharging the battery.

Ozgirgin et al. [19] studied a hybrid system consisting of PV modules, storage batteries, proton exchange membrane (PEM) electrolyzer, and PEM fuel cell. The hybrid system is intended to cover electricity and hot water demand for a residential application of a single household in Ankara, Turkey. The model considered seven cases of PV panel areas and used average global irradiance data for each month to investigate the hybrid system performance for different seasons. They concluded that the hybrid system is effective for powering stand-alone household applications in Ankara.

Modeling, simulation, and optimization of a stand-alone PV-electrolyzer-fuel cell hybrid system to meet a residential community energy demand is presented in Ghenai et al. [20]. Two dispatch control strategies were investigated: load following, in which the system's main objective is to meet the demand, and cycle charging, where the fuel cells operate at maximum capacity to meet the demand and run the electrolyzer as well. The resulted optimum system configuration, which uses the cycle charging control strategy, was able to meet the load demand with a negligible unmet load percentage of 0.08%, low levelized cost of energy of 0.145 \$/kWh, and a CO_2 emission-free electricity generation.

Tebibel et al. [21] presented a hydrogen management strategy to optimize hydrogen production from methanol electrolyzer powered by an off-grid PV-battery system. The system is intended to cover a hydrogen demand for two applications, each with a different demand profile. Measured meteorological solar irradiance and ambient temperature data were acquired for Algiers city, and the off-grid system was simulated for one year at two different PV tilt angles: horizontal and 36° tilt. The tilted position achieved higher PV power production, and hence required less capacities of the individual systems components: PV, electrolyzer, and hydrogen storage tanks.

Cabezas et al. [22] demonstrated that -with proper installation- it is possible to harvest a good amount of solar energy in high latitude regions of Antarctica, which is approximately half the amount harvested in a reference location in Argentina. In their study, two vertical PV modules (facing NE and NW) were installed on a house wall in Antarctica, and the delivered power data were collected for two years. Long-term hydrogen storage system (composed of an alkaline electrolyzer, a PEM fuel cell stack, and storage reservoirs) was incorporated in the system to maintain demand power delivery throughout the sharp seasonal decline in the harvested solar energy.

Integrating renewable power resources, especially wind and PV systems, with battery storage systems has also been established to meet a certain demand load. Hongxing et al. [23] presented an optimal design model for a hybrid PV-WT-Battery system to power a telecommunication relay station on a remote island in China. The model objective was to minimize the annualized cost of the system, while maximizing the system reliability using the weather data of the year 1989 in Hong Kong city.

Baghaee et al. [24] investigated a hybrid wind-solar system with hydrogen energy storage (consisting of an electrolyzer, hydrogen storage tank, and a fuel cell) with the goal of finding the optimal size of the system components that minimizes the system's cost and maximizes its reliability. Wind speed and global irradiance data were acquired for Ardebil province in Iran, and the system was simulated over one year. The simulation yielded a Pareto optimal set for each of the three cases studied; a hybrid system, only solar generation, and only wind generation. For future work, the authors suggested investigating grid-connected renewable energy hybrid systems, since the grid can cover the system power fluctuations economically better than energy storage systems.

Hosseinalizadeh et al. [25] simulated a hybrid system consisting of PV modules, wind turbines, a battery bank, and a hydrogen energy storage system to minimize the total energy costs. The average wind speed and solar irradiance values were used in the simulation for four different regions in Iran. For every region investigated, the problem covered three scenarios: a hybrid PV-WT system, PV only system, WT only system. The use of the hybrid system was proven the optimal scenario for all four regions. The optimal results also proved that utilizing the battery bank as the main storage and the fuel cells for backup purposes was economically favorable.

A sizing optimization problem intended to maximize profitability and minimize environmental hazards is presented in Mukherjee et al. [26]. They proposed a renewable hydrogen-powered microgrid system design to back up the grid and meet the power demand of a community in Ontario, Canada. The system consisted of PV modules, wind turbines, electrolyzers, hydrogen storage tanks, fuel cells, and fuel cells vehicles, which provide vehicle to grid services for backup power generation. For their model, hourly wind and solar irradiance data were acquired for one year. The microgrid system was required to provide at least 10% of the community energy demand under normal operation, while being able to meet the community energy demand for a two-day blackout period (off-grid operation). Their model returned an optimal solution for each of the microgrid system components; however, the system did not achieve a positive net present value at the end of its project life of 20 years due to the scale of the system, even after considering the profits and savings earned by the services offered when implementing the microgrid model.

In this work, an integrated PV-electrolysis-battery system is presented with the goal of identifying optimal system size. The PV modules provide the necessary power to run the electrolyzer, while using the excess power to charge the battery during peak PV power production. The battery will subsequently provide the power necessary to ensure uninterrupted operation of the electrolyzer during night. Diurnal and seasonal weather variations are also included and are used to optimize individual system elements. The system is connected to the electric grid to ensure uninterrupted operation of the electrolyzer during seasonal weather variations. During times where the power generated from the PV modules is insufficient to fully meet the electrolyzer and battery charge/discharge load, power will be supplied by the grid. On the contrary, excess power will be sold to the grid in cases where the power generated by the PV modules exceeds the integrated system power requirements. A schematic diagram of the coupled system is presented in Fig. 1. The simulation is implemented in Python environment, and is run for the calendar year 2017 in College Park city, Maryland.

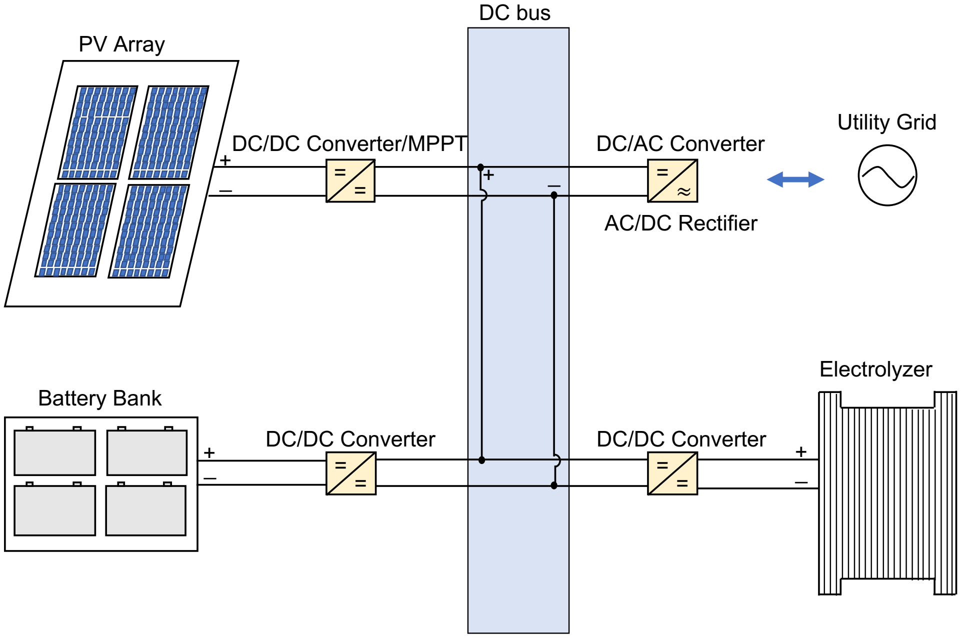

Fig. 1. A schematic diagram of the coupled system.

To achieve maximum design and operation sustainability, the coupled system is required to meets *net-zero* grid energy throughout the whole year. Since the proposed system is designed for commercial-scale applications (with hydrogen production rate in the range 5-120 Normal m^3/h), reaching a value of exactly zero is highly improbable. Instead, the coupled system can be assumed to meet *net-zero* energy when the system meets a cut-off value of $\pm5\%$ relative to the daily plant power consumption. That is, the system's net grid energy (NGE) evaluated at the end of the year shall not exceed 5% of the electrolyzer power consumption in a day.

The analysis goal is to identify the optimal system configuration necessary to maximize the hydrogen production rate, minimize the total annual cost of the system (ACS), minimize the levelized cost of energy (LCE), while meeting an annual grid net-energy within $\pm5\%$ relative to the daily plant power consumption.

Most published research uses meteorological data from nearby weather stations or specialized websites and platforms to get the global solar irradiance, and hence evaluate the dynamic operation and performance of the PV modules. However, these data sets may not be readily available for any location on earth; hence its application worldwide might be limited. This work provides a clear mathematical model to calculate the global irradiance falling on a PV module surface given its orientation, at any location as a function of time of the day. This model has proven to be effective in forecasting the energy generation of a solar-powered house in Colorado during the 10 day competition period in the 2017 US Department of Energy Solar Decathlon (SD) contest, where team Maryland took second place overall and first among US teams. The ability of the model to accurately forecast future energy generation was a key factor behind team Maryland achieving nearly perfect net-zero electrical power performance. During the design, prototype, and construction phases of the reACTHouse (UMD 2017 SD entry), the model was also validated when applied and tested on the LEAFHouse (UMD 2007 SD entry, currently located in UMD campus) to compare the simulation's prediction of house performance to measured LEAFHouse power generation data.

Unlike some research that uses a 24-hour period to simulate and analyze the hybrid system, or assumes a fixed averaged value of global irradiance, this model uses hourly incremented calculations to simulate the coupled system for one year; including both diurnal and seasonal weather variations. The computational platform presented in this article to model integrated solar hydrogen systems can be extended to more complex hybrid systems.

The rest of the paper is organized as follows. Detailed modeling of the integrated system individual components is presented in section 2, and an economic model is then introduced in section 2.5. The problem formulation is presented in section 2.6, and the coupled system model algorithm is explained in section 2.7. Simulation results are presented and discussed in Section 3. Finally, conclusions of this work are summarized in Section 4.

2 Mathematical Model

2.1 Solar Irradiance Modeling

The solar constant G_{sc} (= 1366 W/m^2) is the maximum direct solar irradiation reaching the Earth's surface if none of the radiation is absorbed or scattered by the atmosphere. The effect of Earth's atmosphere is a key factor to consider since a significant fraction of the solar irradiance is either absorbed or scattered by molecules and particles in the atmosphere, leading to the definition of two important irradiance components; direct (G_D) and diffuse (G_F). Direct irradiance refers to the direct sunbeams reaching Earth, while the diffuse component corresponds to the fraction of the solar irradiance scattered by the atmosphere, but eventually reaching the Earth's surface. The global irradiance G_G is then defined as the summation of the direct and diffuse components.

Equation (1) can be used to calculate the global irradiance as a function of location, time of the day, and date [27].

$$G_G(t_d, \phi, \theta) = [(0.11 + \cos\zeta)\, G_{D\perp}] \times H(\cos\zeta) \tag{1}$$

with

$$G_{D\perp} = G_{sc} \times 0.73^{AM^{0.678}} \tag{2}$$

$$AM = \frac{0.89^z}{\cos\zeta} \qquad \text{for } z < 3 \text{ km} \tag{3}$$

$$\cos\zeta = -\vec{n_i} \cdot \vec{s} \tag{4}$$

$$\vec{s} = 0\vec{x} + 1\vec{y} + 0\vec{z} \tag{5}$$

$$\vec{n_i} = n_{x_i}\vec{x} + n_{y_i}\vec{y} + n_{z_i}\vec{z} \tag{6}$$

$$n_{x_i} = \cos\lambda_y \sin\phi \sin\theta_i + \sin\lambda_y \left(\cos\delta \sin\phi \cos\theta_i + \sin\delta \cos\phi\right) \tag{7}$$

$$n_{y_i} = -\sin\lambda_y \sin\phi \sin\theta_i + \cos\lambda_y \left(\cos\delta \sin\phi \cos\theta_i + \sin\delta \cos\phi\right) \tag{8}$$

$$n_{z_i} = -\sin\delta \sin\phi \cos\theta_i + \cos\delta \cos\phi \tag{9}$$

$$ast_i = 24\,(i/n_{ast}) \tag{10}$$

$$\theta_i = 2\pi\,(n_{ast} - i)/n_{ast} - 2\pi\,(t_d/365) \tag{11}$$

$$\phi = 2\pi\,(90^o - \phi^o\text{N})/360^o \tag{12}$$

where $G_{D^\perp}$ is the direct irradiance reaching a surface that is aligned perpendicular to Sun's rays, AM is the effective air mass, ζ is the zenith angle, the angle made between a line segment extending between the Earth and sun and local vertical, z is the site elevation in km, $\vec{n_i}$ is the vector normal to and pointing out of the PV module surface, $\vec{s}$ is the solar radiation vector directed along the y-axis, $\lambda_y = 2\pi t_d/365$ is an angle representing Earth's mean orbit at t_d, t_d is the number of days past the most recent winter solstice, ϕ is the latitude in degrees measured north of the equator, θ is the longitude, δ is the Earth's declination at $t_d = 0$ (equals to 23.44^o), ast is the apparent solar time (with $ast = 12$ at solar noon, and $ast = 0, 24$ at midnight), and H is the Heaviside function and is used to prevent negative irradiance values on the night-side of the planet. Detailed derivation of these equations is provided in [27].

When a PV module is tilted with an angle θ_{tilt} towards the South Pole, $\phi_{tilt} = \phi + \theta_{tilt}$ is used in Equations (7), (8), (9), and (12) instead of ϕ to calculate $\vec{n}_{i,tilt}$ and $\cos\zeta_{tilt}$. The global irradiance can then be calculated from:

$$G_G(t_d, \phi, \theta) = [H(\cos\zeta_{tilt}) G_{D^\perp} \cos\zeta_{tilt} + 0.11 G_{D^\perp}] \times H(\cos\zeta) \tag{13}$$

The $H(\cos\zeta_{tilt})$ term is added to account for cases where the PV module is tilted away from the Sun's radiation during daylight (with $\cos\zeta_{tilt} < 0$ and $\cos\zeta > 0$), and hence only receives the diffuse component of the irradiance.

2.1.1 Effect of Cloud Cover

The above model calculates the global irradiance falling on a PV module surface given its orientation, at any location as a function of time of the day. However, the effect of cloud cover is not yet addressed. For a completely cloudy day, it is reasonable to assume that only the diffuse part of the irradiance constitutes the global solar irradiance, with 20% the intensity of the direct normal irradiance [28]

$$G_{\text{cloudy}} = 0.2 \times G_D^\perp \tag{14}$$

Since the clouds cover is typically represented as a fraction between 0 and 1, a simple weighted average is assumed such that the irradiance value is equal to G_G for sunny days ($CloudsCover = 0$), and G_{cloudy} for a completely cloudy day ($CloudsCover = 1$).

$$G_{\text{total}} = CloudsCover \times G_{\text{cloudy}} + (1 - CloudsCover) \times G_{\text{G}} \tag{15}$$

It should be noted that there are different and more complex models to estimate the cloudy days irradiance, often requiring the incorporation of many metrological parameters, and the research is still underway to optimize and enhance the accuracy of these models. Nevertheless, it has been shown in the literature that the very simple cloudy sky irradiance models performed comparably to the complex ones [29].

Hourly weather data for the 2017 year is acquired by executing an API request from the Dark Sky API website [30]. Hourly cloud cover data then can be extracted from the weather data. Fig. 2(a) and Fig. 2(b) provide the cloud cover data for College Park, MD for the first week of January, and the first week of August, respectively, compared to the total solar irradiance calculated G_{total}, showing the inverse correlation between the two. Comparing the two weeks in Fig. 2 shows the effect the time of the year has on the value of the total solar irradiance, with noticeable lower irradiance values in winter, Fig. 2(a), compared to summer, Fig. 2(b). Hourly cloud cover data and the total solar irradiance, G_{total}, for the entire year 2017 are provided in Fig. S1 of the supplementary material. A list of the input parameters and variables used in the model is given in Table S1 of the supplementary material.

It should be noted that, whenever available, minutely data provide a more accurate solar irradiance representation compared to hourly data, and hence, can reflect rapid real-life power fluctuations due to rapid variations in solar irradiance occurring within the hour [31, 32]. However, for extended period of time, e.g. one year, the difference in hourly and minutely irradiance simulations can be trivial [32].

2.2 PV Module Characteristics

The PV module considered in this work is the SunPower SPR-X21-345 [33], which consists of 96 solar cells connected in series. If each cell in the module performs identically, the module

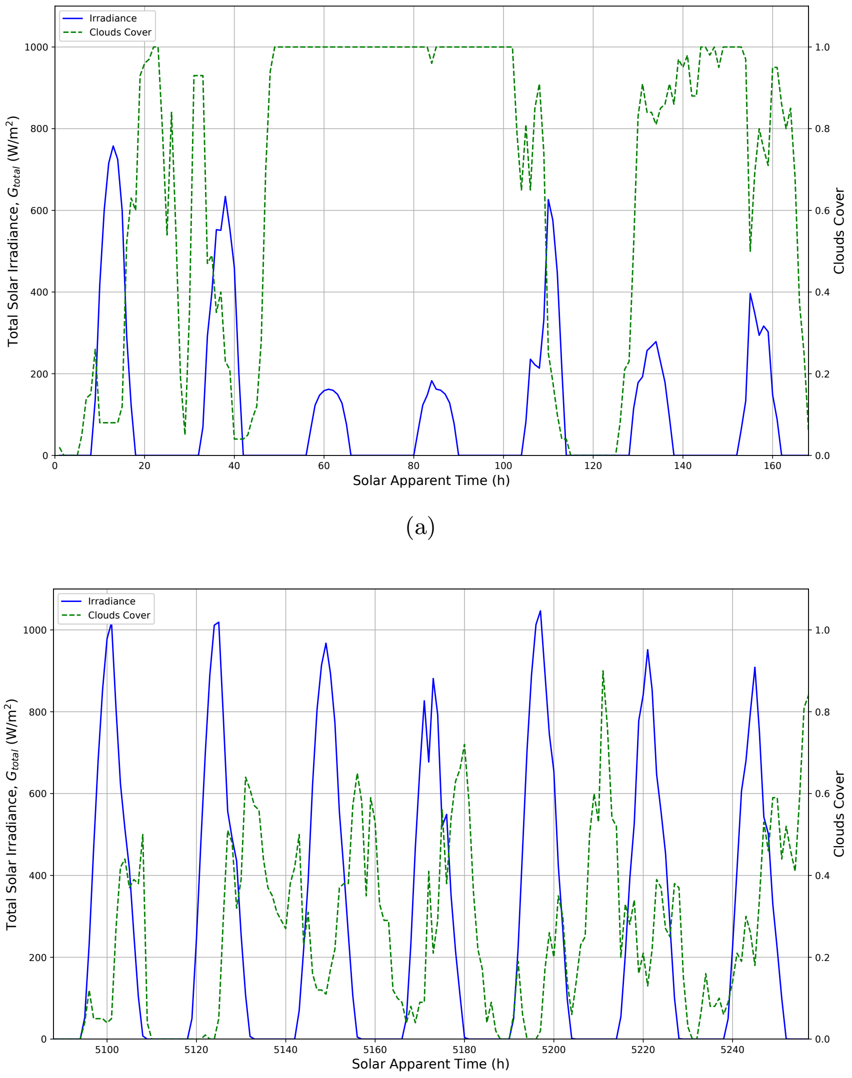

(a)

(b)

Fig. 2. Hourly cloud cover data from Dark Sky API for College Park, MD and the solar irradiance G_{total} calculated at a module tilt angle of 35° for the first week of January (a) and the first week of August (b).

performance model can be written in terms of the diode equation

$$I = -I_{ph}X(t) + I_o\left[\exp\left(q\frac{V/96 - IR_s}{\beta k_B T}\right) - 1\right] + \frac{V/96 - IR_s}{R_{sh}} \tag{16}$$

where $X(t)$ is the dimensionless concentrating factor proportional to the global irradiance so that $X(t) = G_{\text{total}}(t)/(1000\ \text{W/m}^2)$. The diode ideality factor $\beta \in [1, 2]$ approaches unity under ideal performance conditions. The series R_s and shunt R_{sh} resistances approach 0 and positive infinity, respectively, for an ideal PV cell. I_o and I_{ph} are the dark saturation and photo-currents, respectively.

An iterative non-linear procedure is used to fit the manufacturer module specifications at the short circuit, open circuit, and maximum power points. The diode equation parameter values are identified as a result of the fitting procedure and are shown in Fig. 3 and presented in Table 1. These parameters are then substituted in the diode equation (16) to determine the $I - V$ and $P - V$ characteristic curves at each point during the day according to the different value of the concentration factor $X(t)$.

Table 1. SunPower SPR-X21-345 module parameter fitting results on a per-cell basis.

I_{ph} (A)	I_o (A)	R_s (Ω)	R_{sh} (Ω)	β
6.39	6.28×10^{-12}	6.70×10^{-3}	2.00×10^{3}	1

PV systems are ideal power supplies for electrolyzers. This is mainly because the output voltage of the PV modules can be controlled to relatively constant values as illumination levels change. This is particularly valuable for fast transients, such as the sudden reduction of irradiance due to a passing cloud. Furthermore, the use of a DC-DC converter and optimizer ensures that the output power is at the maximum power point (P_{mp}, V_{mp}, I_{mp}). In this analysis, the electrolyzer is assumed to follows a constant-current operational mode, which requires a constant and steady source of voltage. Hence, the mean value of the non-zero entries throughout the year ($V_{mp,mean}$) is chosen as the operating voltage of the electrolyzer. Fig. S2 shows non-zero values of the V_{mp} (i.e., during daylight operation of the PV module) for the year, with the mean value $V_{mp,mean}$ calculated to be 55.6 V.

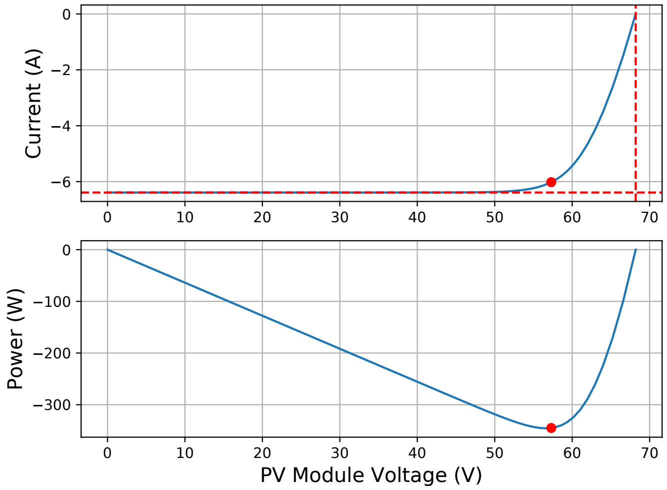

Fig. 3. SunPower SPR-X21-345 Module parameter fitting results (the negative sign corresponds to power produced by the PV module). The maximum power point is denoted in red.

2.3 Electrolyzer Design

A bipolar alkaline water electrolysis unit is considered in this work. In bipolar designs, the active electrodes (positive and negative) are connected to different sides of a conducting metal plate (or a bipole), and they are geometrically and electrically connected in series [8, 34]. A bipolar stack consisting of N cells wired in series typically operates at higher voltages and lower currents, hence, multiple stacks M connected in parallel are required for large-scale applications.

Conventional alkaline electrolyzers typically operate at pressures of 1-30 bar and temperatures between 70 to 100° C [34]. Most commercial alkaline electrolyzers operate at 80° C [14, 34, 35]. Water is nominally split at current densities between 100 to 400 mA/cm^2 in an aqueous KOH electrolyte with concentrations between 25-35 wt% [36]. Higher current densities are avoided as they will increase internal ohmic losses due to the electrolyte [8, 36].

The diaphragm choice has critical implications for the electrolyzer design and operation. The diaphragm must have high ionic conductivity, while being stable in strong alkaline solutions and high temperatures. For this work, Zirfon Perl [37], a high quality separator membrane for alkaline water electrolysis, is chosen. This membrane is durable in strong alkaline solutions (up to 6 M KOH), and up to 110° C. It has a high number of OH$^-$ groups at alkaline pH and low ionic resistance (0.3 Ωcm^2 at 30° C in 30 wt% KOH [37]), allowing higher current values to be reached.

2.3.1 Electrolysis Cell Characteristics

In previous work [38], the mechanism and kinetics of both OER and HER were investigated on nickel-iron layered double hydroxide (NiFe LDH) films deposited on Ni foam substrates. The results and analysis of linear sweep voltammetry and electrochemical impedance spectroscopy were combined to reveal valuable insight on the reaction kinetics and mechanism occurring at each electrode. The results identified from the anode and the cathode were then combined to fit the electrochemical cell experimental data.

Now that the electrolyzer design is set, the electrolysis cell characteristics at the nominal set of design parameters can be investigated. It is well known that most reaction rate constants of solution reactions vary with temperature according to Arrhenius law. The electrolyzer is assumed to operate at 80° C; hence, Arrhenius law ($\ln k \propto -1/T$) can be used to recalculate the values of the partial standard reaction rate constants reported in [38], that were originally evaluated at room temperature.

In addition to its effect on the reaction kinetics, temperature has a crucial influence on the electrolyte resistivity: higher temperatures promote higher ionic conductivity in the electrolyte. A 25 wt% KOH electrolyte at 80° C has an ionic conductivity of 1.302 S/cm [39]. With a 5 mm electrolyte path and 0.5 m^2 electrode area, the electrolyte total ohmic resistance can be calculated as the summation of the solution and membrane resistances, and is equal to $1.368 \times 10^{-4}\ \Omega$.

The electrolysis cell $I - V$ characteristics can be expressed using Equation (17)

$$V_{\mathrm{cell}} = 1.23 + \eta_{\mathrm{a}} + \eta_{\mathrm{c}} + I_{\mathrm{cell}} \times R_{\Omega} \tag{17}$$

where η_{a} and η_{c} are the anode and cathode overpotentials, respectively, and R_{Ω} is the cell ohmic resistance. The resulting $I - V$ curve is shown in Fig. 4.

2.3.2 Power of the Electrolyzer

For a fixed N cells wired in series, and M stacks connected in parallel, the total power of the electrolyzer at any time is equal to:

$$P_e = M \times N \times V_{\mathrm{cell}} \times I_{\mathrm{cell}} \tag{18}$$

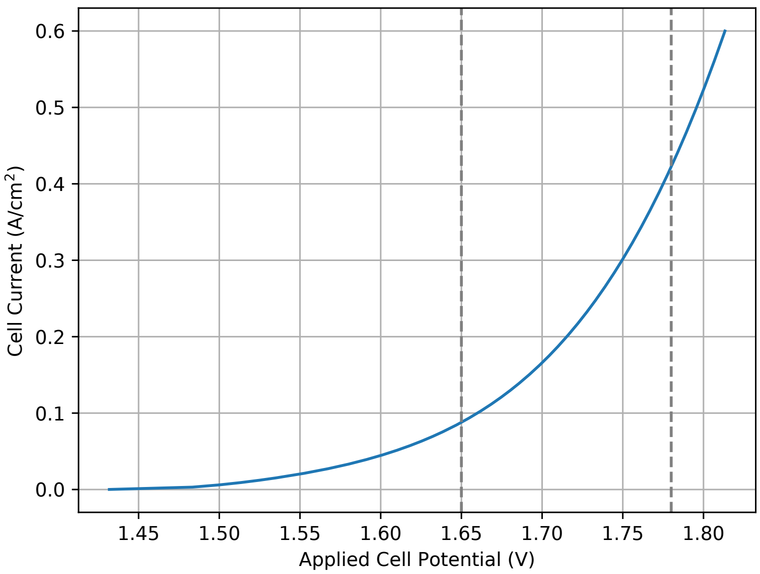

Fig. 4. Current-voltage characteristics of the electrolysis cell at 80 C. The dash lines define the electrolysis cell operating range, approximately between 100-400 mA/cm^2.

The total hydrogen production rate (mol/s) can be calculated from:

$$n_{\mathrm{H}_2} = \frac{M \times N \times I_{\mathrm{cell}}}{2 \times F} \tag{19}$$

Gas flow rates are typically reported as normal cubic meters per hour (Nm^3/h). The volumetric production rate can be calculated using [34]:

$$V_{\mathrm{H}_2} = n_{\mathrm{H}_2} \times \nu_{std} \times 3600 \tag{20}$$

where ν_{std} is the volume of an ideal gas at standard conditions.

2.4 Battery Design

A battery model is proposed in (21), which is simple yet capable of accurately predicting the stored battery energy at any point in time. The electrolyzer unit is assumed to be operating at constant current mode, therefore, for a fixed system size, the battery state of charge (SOC) is solely dependent on the solar irradiance and weather conditions. The battery, therefore, will only charge when the PV modules are producing excess power and is required to discharge when the PV power is insufficient to operate the electrolyzer system. Considering a lead acid battery with a round-trip efficiency η_b of 85% [40], the battery operation can be expressed from an energy standpoint:

$$\frac{dE_b}{dt} = \begin{cases} \eta_b \left(P_{PV}(t) - P_e(t)\right), \; P_{PV}(t) \geq P_e(t) \\ \left(P_{PV}(t) - P_e(t)\right), \; P_{PV}(t) < P_e(t) \end{cases} \tag{21}$$

with

$$SOC(t) = \frac{E_b(t)}{Cap} \times 100 \tag{22}$$

where E_b is the energy stored in the battery, Cap is the battery capacity, and P_{PV} and P_e are the PV power produced, and electrolyzer power consumed, respectively. The first case in (21) corresponds to a charging state, and the second case is a discharging state. To extend the life of a lead acid battery, it should not be completely depleted. Instead, a minimum limit on the battery energy should be applied. The battery depth of discharge (DoD) is defined as the percentage of the discharged energy of the battery to the total battery capacity. In this model, a DoD of 70% is applied as the minimum limit constraint on the battery [41].

2.5 Economic Model

2.5.1 System Cost

Our economic model is derived from the annualized cost of the system (ACS), which mainly consists of the annualized costs of PV ($C_{\mathrm{a,pv}}$), electrolyzer ($C_{\mathrm{a,e}}$), and battery ($C_{\mathrm{a,bat}}$). The cost of grid electricity ($C_{\mathrm{a,grid}}$) also is included in the analysis. The costs of electrical converters are not included in this analysis as these costs represent only a small fraction (<1%) of the total systems cost [15].The ACS can be calculated using:

$$ACS = C_{\mathrm{a,pv}} + C_{\mathrm{a,e}} + C_{\mathrm{a,bat}} + C_{\mathrm{a,grid}} \tag{23}$$

For each component in the coupled system, the annualized cost is the summation of the capital cost (C_{aCapital}), replacement cost (C_{aRep}), and the operation and maintenance cost ($C_{\mathrm{aO\&M}}$). Hence, the total annualized cost of the j^{th} component can be written as:

$$C_{\text{a},j} = C_{\text{aCapital},j} + C_{\text{aO\&M},j} + C_{\text{aRep},j} \tag{24}$$

The annualized capital cost for the PV modules and the electrolyzer can be calculated using [23]

$$C_{\text{Capital},j} = U_j \times P_j \tag{25}$$

$$CRF_j = \frac{i(1+i)^{n_j}}{(1+i)^{n_j}-1} \tag{26}$$

$$C_{\text{aCapital},j} = C_{\text{Capital},j} \times CRF_j \tag{27}$$

where the subscript j is used to denote the component (PV, electrolyzer). $C_{\text{Capital},j}$ is the capital investment and installed cost ($), U_j is the unit capital cost ($/kW), P_j is the power produced or consumed (kW), CRE_j is the capital recovery factor (necessary to calculate the annual worth from the present value), i is the real discount rate, and n_j is the lifetime of the j^{th} component. P_{pv} is the nominal power produced by each module (=0.345 kW [33]) multiplied by the number of PV modules (M_{pv}).

For the battery capital cost, P_j in Equation (28) is replaced with the battery capacity (Cap), and the unit capital cost U_{bat} is given in $/kWh:

$$C_{\text{Capital,bat}} = U_{\text{bat}} \times Cap \tag{28}$$

$$CRF_{\text{bat}} = \frac{i(1+i)^{n_{\text{bat}}}}{(1+i)^{n_{\text{bat}}}-1} \tag{29}$$

$$C_{\text{aCapital,bat}} = C_{\text{Capital,bat}} \times CRF_{\text{bat}} \tag{30}$$

The annualized O&M costs for the PV modules and the electrolyzer can be determined from:

$$C_{\text{aO\&M},j} = U_{\text{O\&M},j} \times P_j \tag{31}$$

The battery annualized O&M cost is:

$$C_{\mathrm{aO\&M,bat}} = U_{\mathrm{O\&M,bat}} \times Cap \tag{32}$$

In this work, the project lifetime is assumed to be equal to the PV system lifetime of 30 years [42], hence, no replacement cost is considered for the PV system. Alkaline electrolysis plants have a lifetime up to 30-50 years; however, stack replacements are often required before reaching this lifetime [43]. Most state-of-art commercial alkaline electrolyzers have a stack lifetime between 78,840 and 96,000 hr, equivalent to 9.2-11.2 years (with 8,585 operational hour per year) [44, 45]. Considering a stack lifetime of 10 years, replacements are required twice during the lifetime of the project. With a stack replacement cost of 50% of the capital installed cost [44], the annualized replacement cost is calculated using:

$$C_{\mathrm{Rep,e}} = RF_{\mathrm{Rep,e}} \times C_{\mathrm{Capital,e}} \tag{33}$$

$$C_{\mathrm{aRep,e}} = CRF_e \times \left(C_{\mathrm{Rep,e}}(1+i)^{-10} + C_{\mathrm{Rep,e}}(1+i)^{-20}\right) \tag{34}$$

where RF is the replacement cost factor. In Equation (34), this factor $(1+i)^{-n}$ is used to convert the future payments at year n (i.e. replacement cost) to its present worth, before multiplying it by CRF to convert it to its annual worth value (in \$/yr). Lead-acid batteries typically have a lifetime of 15 years [40], after which the battery bank is replaced. It should be noted that in practice, the battery lifetime can be less as it depends on the battery operating conditions and specifications [46]. Different models are available in the literature that predicts the battery lifetime [46], however; this requires detailed battery operational condition and specifications and is out of the scope of this work. With an assumed battery lifetime of 15 years and a replacement factor (RF) of 100%, the annualized replacement cost can be calculated using Equation (36). The economic parameters used in this analysis are given in Table 2. The costs of electrical converters are not included in this analysis as these costs represent only a small fraction of the total system's cost [15].

$$C_{\mathrm{Rep,bat}} = RF_{\mathrm{Rep,bat}} \times C_{\mathrm{Capital,bat}} \tag{35}$$

$$C_{\mathrm{aRep,bat}} = CRF_{\mathrm{bat}} \times C_{\mathrm{Rep,bat}}(1+i)^{-15} \tag{36}$$

Table 2. The economic parameters used in this analysis. A real discount rate i of 6.9% is assumed in this analysis for 2017 [42].

	PV	Electrolyzer	Battery
U_j	1850 (\$/kW) [42]	1300 (\$/kW) [43]	500 (\$/kWh) [40]
$U_{\mathrm{O\&M},j}$ (/year)	21 (\$/kW) [42]	2.5% $\times U_{\mathrm{e}}$ (\$/kW) [43]	3% $\times U_{\mathrm{bat}}$ (\$/kWh) [23, 41]
n_j (year)	30 [42]	10 [44]	15 [40]

The U.S. Energy Information Administration reported the cost of electricity for commercial applications in the state of Maryland of 0.1075 \$/kWh [47]. Hence, to calculate the grid annualized cost, the cost of electricity is multiplied by the net-energy consumption for the year:

$$C_{\mathrm{a,grid}} = 0.1075 \times \text{Net Energy} \tag{37}$$

$C_{\mathrm{a,grid}}$ can either take a positive or a negative value, depending on the sign of the yearly net-energy balance for each configuration considered in the optimization study. A positive sign of the net grid energy is assigned when excess energy is sold to the grid, and negative for energy supplied by the grid.

2.5.2 Levelized Cost of Energy

The levelized cost of energy (LCE) is a concept frequently discussed when comparing alternative energy-producing systems, particularly with renewables such as solar or wind. It also is used as a benchmark to evaluate different system sizing combinations and to determine the optimal size. LCE can be defined as the cost associated with producing 1 kWh of energy. It can be calculated by dividing the total annualized costs of the hybrid system (\$/yr) by the total energy produced by the PV system (kWh/yr) [48]:

$$LCE = \frac{C_{\mathrm{a,pv}} + C_{\mathrm{a,bat}}}{E_{\mathrm{an}}} \tag{38}$$

2.6 Problem Formulation

In this work, we seek to model, simulate, and optimize the coupled system with the goal of maximizing hydrogen production rate while minimizing the total cost associated with the system size. This implicitly requires finding the right sizing combination of the system's components necessary to ensure high hydrogen production rate, while minimizing excess power production and system physical dimensions. To promote sustainability, the optimal solution will be required to have an annual net-grid energy balance that falls within ±5% relative to the daily plant power consumption. In addition to minimizing the combined system cost, minimizing the LCE also is included to ensure the optimality of the solution.

The Pareto Frontier analysis is used to generate the optimal solutions of the multi-objective optimization problem. The Pareto-Frontier is a set of non-dominated solutions and is typically generated for multi-objective optimization problems, where finding a single best solution is improbable. This concept, formulated by Vilfredo Pareto, is one of the earliest in multi-objective optimization field [24, 49]. Its simplicity and effectiveness in finding the solution space is one of its main advantages. Due to the complexity and high-depth of the mathematical model used to describe the coupled system, a simple and effective Pareto-Frontier analysis was a legitimate approach in this study.

The optimization variables considered are the number of PV modules connected in parallel (M_{pv}), number of electrolysis cells in each stack (N), number of stacks in the electrolyzer unit (M), and battery capacity (Cap).

To lower system losses associated with the cell ohmic resistance, conventional alkaline electrolyzers typically operate at current densities between 100-400 mA/cm^2 [8, 36]. This operating range defines upper and lower bounds on the number of cells N connected in series in an electrolyzer stack. At this operating range of current densities, the design voltage for each cell should be kept between 1.65-1.78 V, as seen in Fig. 4. Hence, for the coupled system sizing optimization purposes, a feasible set of N values is defined as:

$$\frac{V_{mp,mean}}{1.78} \leq N \leq \frac{V_{\mathrm{mp,mean}}}{1.65} \tag{39}$$

This results in a feasible set of N values of 32, 33, and 34 cells connected in series. The design variables values, given in Table 3, define a set of 2,364,120 possible configurations to consider in the optimization problem. The chosen M_{pv} and Cap ranges are intended to cover the maximum and minimum electrolyzer power demand at the ranges of N and M presented in Table 3.

Table 3. Range and step size of decision variables considered in the optimization problem

	N	M	M_{pv}	Cap (kWh)
Minimum value	32	1	100	250
Maximum value	34	10	10000	20000
Step size	1	1	50	50

2.7 Coupled System Model Algorithm

After acquiring the cloud cover data for a specific year, the irradiance model is run to evaluate the concentration factor X, which can be used in the PV diode equation to calculate hourly values of V_{mp}, I_{mp}, and P_{mp} for the entire year. The search space is initialized based on the variables given in Table 3. $V_{mp,mean}$ is used along with an input value of N to evaluate the electrolysis cell operating voltage (V_{cell}), which determines the operating current (I_{cell}) based on Fig. 4. The electrolyzer total operating power (P_{e}) and the hydrogen production rate ($V_{\mathrm{H_2}}$) are then evaluated using Equations (18) and (20).

For each point in the search space, the algorithm proceeds as a loop with incremental hourly time-steps for the entire year. At each time, the battery operating state and energy level are evaluated using (21), with an initial SOC value of 50% at t=0.

Battery model initial conditions are defined by setting the maximum and minimum operating limits for the investigated size ($E_{\mathrm{bat,max}} = Cap$, $E_{\mathrm{bat,min}} = (1 - DoD) \times Cap$). For each time step, if $P_{\mathrm{pv}} \geq P_{\mathrm{e}}$, then the battery is charging, and the charge level at the next point in time is calculated using (21). Before moving to the next time step, we check if the new battery charge is greater than the battery capacity, if so, the excess power will be sold to the grid, assuming a converter efficiency η_{cov} of 90%. If $P_{\mathrm{pv}} < P_{\mathrm{e}}$, the battery is in discharge mode, and the new charge level at the next time step is calculated accordingly. The next charge level is checked against the minimum charge constraint to ensure the battery is not depleted beyond the 70% DoD assigned; if this is the case, power must be supplied by the grid (with a 90% converter efficiency). The net grid energy NGE is evaluated at the end of the year, and the annual relative net grid energy $RNGE$ is then calculated using

$$RNGE = 100 \times \frac{NGE}{24 \times P_e} \tag{40}$$

The cost analysis then is performed to determine the total annualized system cost (ACS) and the levelized cost of energy LCE associated with each size. Fig. 5 presents a flowchart of the algorithm implemented for each sizing combination considered in the optimization process.

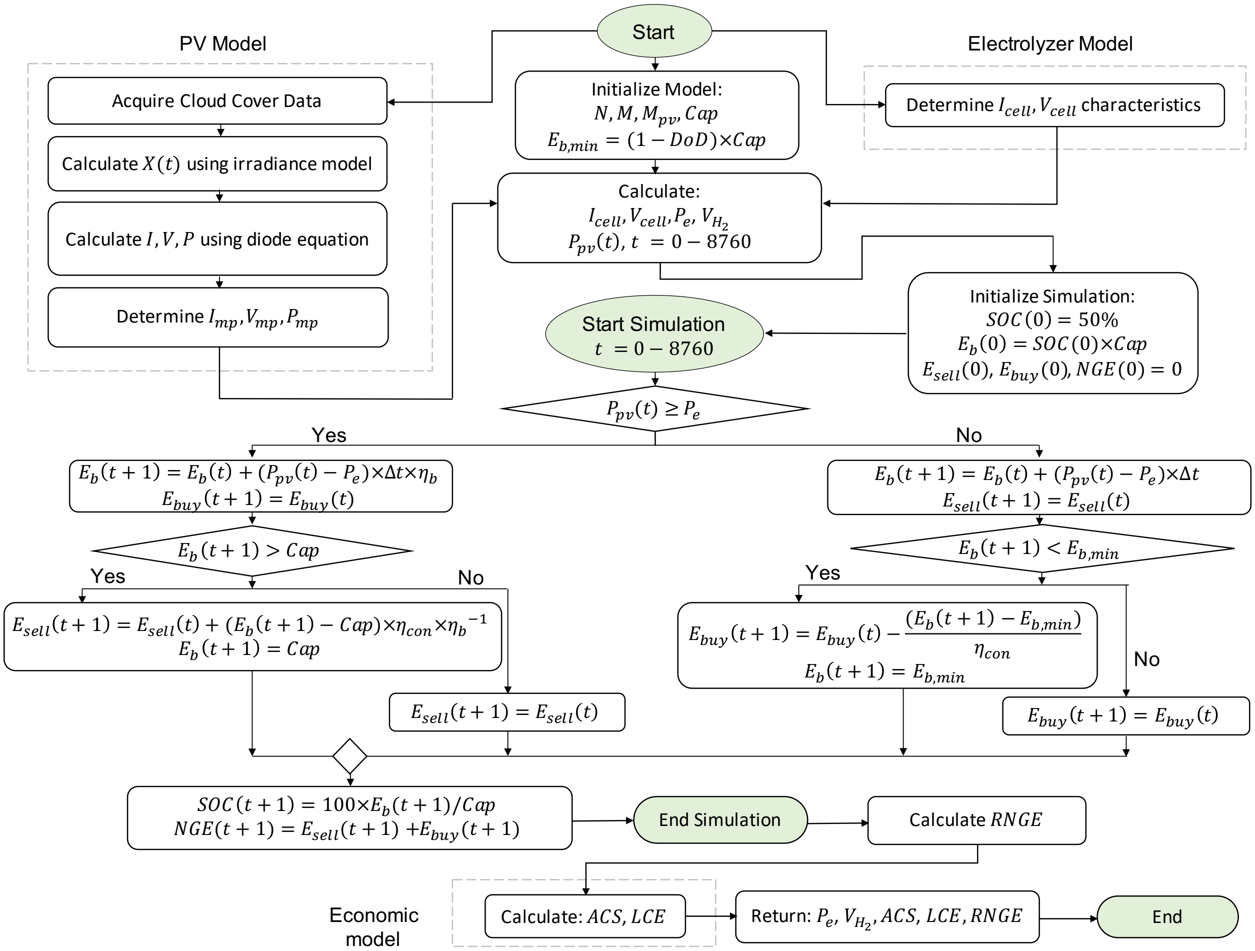

Fig. 5. Flowchart of the algorithm used for each sizing combination considered in the optimization problem.

For each sizing combination investigated, a constraint on the battery capacity is applied, in which the capacity should be able to provide continuous operation of the electrolyzer for at least 12 continuous hours when fully charged. This is to ensure the feasibility of the solution based on our analysis goal. Minimizing the system cost might force the algorithm to choose a size where the battery capacity is too small compared to the plant hydrogen production capacity. These cases correspond to situations where the battery is only able to provide continuous operation for a few hours, i.e., only one or two hours of operation. This case will require purchasing enormous amounts of energy from the grid, which can off-set limited battery capacity on days with high irradiance. To illustrate, the small battery size compared to the power generated by the PV modules will allow it to fully charge rapidly, and the excess energy will be sold back to the grid, resulting in a net-zero grid energy. However, we aim to avoid these scenarios since they contrast the objective of this work, which is to only rely on the grid power in rare cases where the weather variations have substantial influence on the output power of the PV modules.

The optimization problem's search space was refined as the simulation progresses. Because the main target is to achieve an annual net grid energy balance ($RNGE$) within $\pm 5\%$ relative to the daily plant power consumption, redundant size combinations were eliminated during the simulation process. A cut-off value on the $RNGE$ of $\pm 100\%$ was applied to eliminate redundant configurations and to reduce simulation time. For example, if a specific size combination (N, M, M_{pv}, Cap) resulted in a high negative value of $RNGE$ ($RNGE < -100\%$), the electrolyzer designs with greater power consumption (higher values of M) are ignored for this combination. In other cases where the simulation of a specific size combination demonstrated a high positive net-grid energy ($RNGE > 100\%$), higher values of M_{pv} are ignored for this combination . In addition, for infeasible designs where the battery capacity does not meet the minimum requirement to power the electrolyzer for 12 continuous hours, lower values of capacities are considered redundant, and hence, can be ignored. With this, only 6.3% feasible size combinations were simulated among the 2,364,120 set.

2.8 Dimensionless Performance Indicators

To further characterize and evaluate the system's performance, the following performance indicators are used:

- The solar to hydrogen (STH) conversion efficiency is one of the most important factors in evaluating the performance of solar-hydrogen production systems. STH can be calculated using [9]:

$$STH = \frac{N \times I_e(mA) \times 1.23V}{A_{PV_t}(m^2) \times Irradiance(W/m^2)} \tag{41}$$

$$I_e = M \times I_{cell} \tag{42}$$

$$A_{PV_t} = M_{PV} \times A_{PV} \tag{43}$$

  where I_e is the electrolyzer current, I_{cell} is the electrolysis cell current (provided in Fig. 4), A_{PV_t} is the total area of the PV modules used, A_{PV} is the area of a single PV module (1.63 m^2 for SunPower SPR-X21-345 [33]). The annual STH value is then calculated as the average of the hourly STH values [12].

- The satisfied load fraction (SLF) is the ratio of the energy generated by the system sent to the load, relative to the required energy of the load [50, 51]. SLF can be computed using [50, 51]:

$$SLF = \frac{E_{tl}}{E_{ect}} = \frac{E_{pv,tl} + E_{bat,tl}}{E_{ect}} \tag{44}$$

  where E_{ect} is the annual energy required by the electrolyzer, E_{tl} is the annual energy sent to the load (electrolyzer), $E_{pv,tl}$ is the annual energy produced by the PV system that is sent to the load, $E_{bat,tl}$ is the annual energy supplied by the battery to the load.

- The utilization factor (UF) of the energy produced is the ratio of the energy produced by the PV-Battery system that is sent to the load relative to the annual energy produced by the system [50, 51]. The UF is given as [50, 51]:

$$UF = \frac{E_{tl}}{E_{an}} = \frac{E_{pv,tl} + E_{bat,tl}}{E_{an}} \tag{45}$$

  where E_{an} is the annual energy generated by the PV modules during the entire year.

- The grid energy interaction factor ($GEIF$) is the sum of the energy sold to the grid (E_{tg}) and purchased from the grid (E_{fg}) relative to the required energy of the load (E_{ect}) [50, 51].

It provides a measure of the system's interaction with the grid. $GEIF$ is calculated from [50, 51]:

$$GEIF = \frac{|E_{tg}| + |E_{fg}|}{E_{ect}} \tag{46}$$

3 Simulation Results

3.1 Optimal System Size

The simulation results yielded 170 sizing combinations with annual net grid energy ($RNGE$) within ±5% relative to daily electrolyzer power consumption. Among these solutions, 10 were chosen as the Pareto-Frontier for the multi-objective optimization problem and are shown in Fig. 6. Each point in Fig. 6 corresponds to a specific size and is labeled to denote the system components' size combination. The 10 Pareto points are reported in Table 4. The annual dimensionless performance indicators evaluated for the optimal Pareto points are also listed in Table 4.

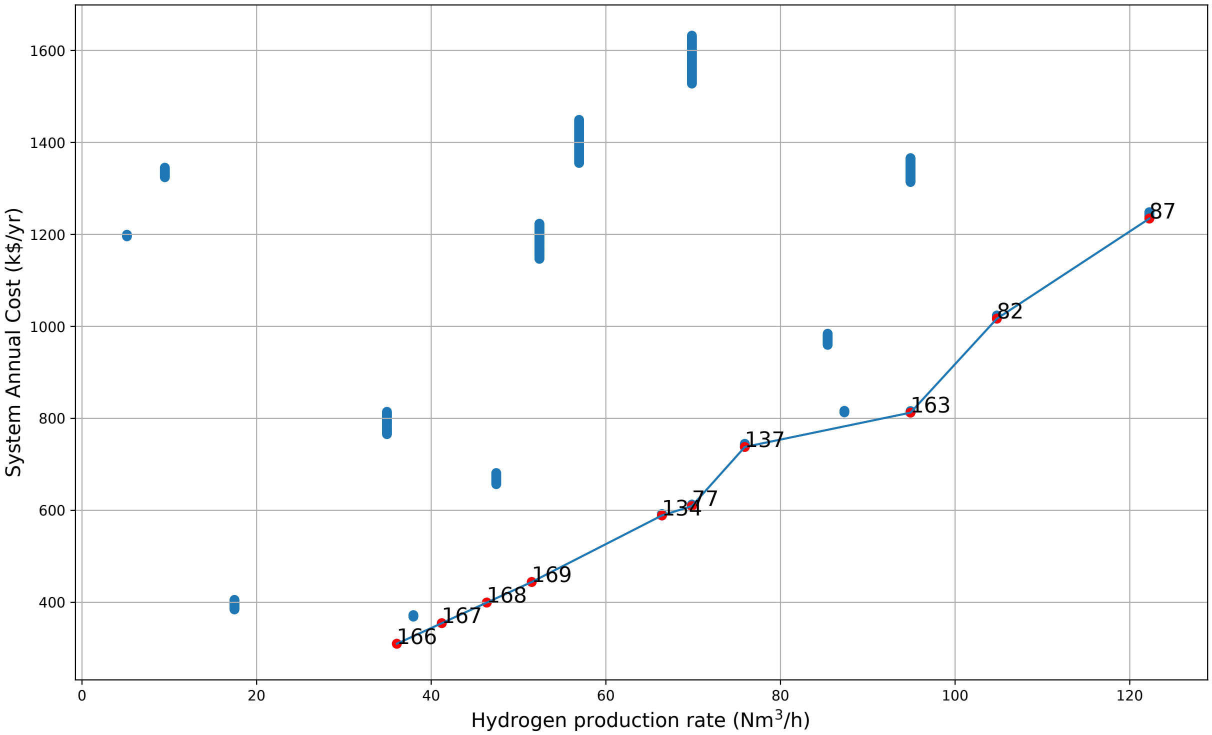

Fig. 6. Hydrogen production rate and total annual system cost for the 170 configurations with a yearly relative net grid energy within ±5% relative to daily power consumption, showing the 10 Pareto-Frontier points. The numbered points are the Pareto optimal solution and are listed in Table 4.

Table 4. The set of Pareto points optimizing the multi-objective problem in this analysis.

Point ID	N	M	Cap (kWh)	M_{pv}	P_e (kW)	$V_{\mathrm{H_2}}$ ($\mathrm{Nm^3/h}$)	ACS (k\$/y)	LCE (\$/kWh)	$RNGE$ (%)	NGE (kWh)	STH (%)	SLF	UF	$GEIF$
77	32	4	3800	5050	290.5	69.9	609.3	0.197	-3.40	-237.2	7.021	0.688	0.617	0.595
82	32	6	7200	7550	435.7	104.8	1016.8	0.222	-4.56	-476.6	7.025	0.751	0.676	0.458
87	32	7	9100	8800	508.3	122.2	1234.5	0.232	-3.58	-436.3	7.022	0.775	0.698	0.418
134	33	7	3900	4650	267.8	66.4	589.0	0.207	-1.88	-121.1	7.243	0.715	0.643	0.534
137	33	8	5400	5300	306.1	75.9	737.9	0.230	-3.65	-267.9	7.240	0.771	0.694	0.424
163	33	10	5150	6650	382.6	94.9	812.5	0.199	-1.70	-156.4	7.238	0.695	0.624	0.579
166	34	7	2050	2450	141.1	36.1	310.0	0.207	-2.94	-99.6	7.462	0.715	0.642	0.536
167	34	8	2350	2800	161.3	41.2	354.8	0.207	-1.35	-52.4	7.462	0.716	0.643	0.534
168	34	9	2650	3150	181.4	46.4	399.5	0.208	-0.12	-5.2	7.462	0.716	0.643	0.533
169	34	10	2950	3500	201.6	51.5	444.3	0.208	0.86	41.8	7.462	0.717	0.644	0.532

The solar to hydrogen (STH) efficiency of the optimum Pareto set ranges from 7 to 7.5% as seen in Table 4. It can be noticed from Table 4 that the optimal points with the same number of electrolysis cells connected in series (N) have similar STH. This is expected because when M is increased, M_{pv} and Cap must also increase by approximately the same factor to ensure the optimality of the new size, and hence STH (given in Equation 41) remains constant. Similar conclusion is also discussed in section 3.3.

Looking at Table 4, the maximum SLF value is equal to 0.775. This value indicates that the PV-Battery system is able to meet 77.5% of the annual electrolyzer energy requirement, and the balance is provided by the grid. An SLF value of 1 indicates that all the annual energy requirements of the electrolyzer are satisfied by the PV-Battery system, which supports off-grid operation of the system. The maximum UF among the optimal Pareto set was 0.698, indicating that 69.8% of the annual renewable energy produced in the PV system is being utilized to meet the electrolyzer energy requirements, and the rest is being stored in the battery at the end of the simulation or sold to the grid. The $GEIF$ of the Pareto points ranged between 0.418 and 0.595. Note that this factor indicates both interactions: energy sold and energy purchased to and from the grid. For optimal energy utilization in off-grid operations, it is recommended to maximize SLF and UF (to approach 1), and minimize the $GEIF$ (to approach 0). This can be achieved by increasing the system storage capacity (i.e. battery capacity). This will reduce the dependency of the system on the grid and ensure that power is only withdrawn from the grid at sever cases, which will take the system a step closer to off-grid operations.

Fig. 6 reveals a clear trade-off between the two conflicting objectives: maximizing the hydrogen production rate requires higher system cost. This result is expected since higher plant capacity requires more energy input, hence, higher system physical dimensions. Because this is a mixed-integer optimization problem in which some of the decision variables can only take integer values, the Pareto Front plotted in Fig. 6 is not smooth. A refined smoother line can be obtained as the step size of the decision variables approaches zero. However, because of the non-linear relation between I_{cell} and V_{cell} and their dependency on N, a completely smooth or straight line is highly improbable.

Fig. 7 shows that higher hydrogen production rates yield lower LCE. Since increasing the hydrogen production rate requires higher input energy (E_{an}), LCE value will decrease according

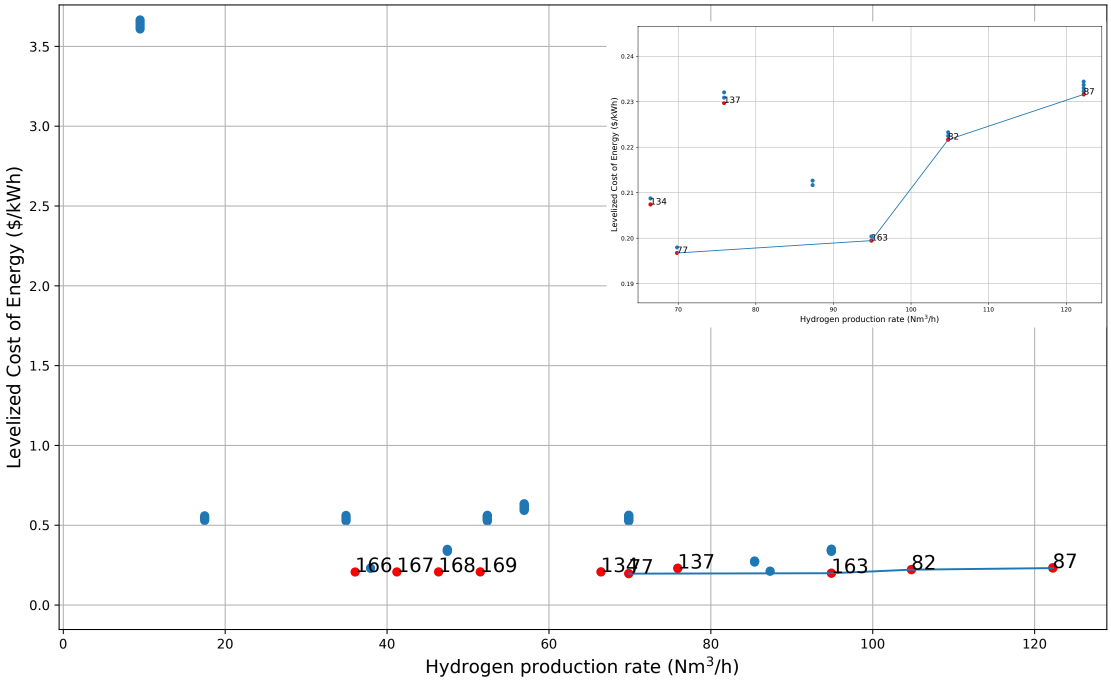

Fig. 7. LCE and Hydrogen production rate for the configurations with an annual net grid energy within ±5% relative to daily power consumption. The insert shows a closer look on the Pareto Front. The numbered points are the Pareto optimal set and are listed in Table 4.

to Equation (38). It should be noted that the increase in (E_{an}) exceeds the observable increase in the PV and battery costs, resulting in a decline in the LCE as the system's physical dimensions increase. However, at high hydrogen production capacities, the increase in required battery capacity leads to higher system costs, which can exceed the increase in the annual energy produced throughout the year. Supporting evidence for this conclusion is provided by the slight increase in the LCE value in Fig. 7 between points 77, 163, 82, and 87. These points are the optimal solution for this graph as they maximize V_{H_2} while minimizing LCE, and they are already a subset of the Pareto Front reported in Table 4. The trade-off between the ACS and LCE results in the Pareto front shown in Fig. 8, which is a subset of the Pareto set reported in Table 4. This implies that optimizing the system's cost and hydrogen production rate implicitly ensures the LCE is also minimized.

3.2 Optimal Sizing and Relative Net-Grid Energy

Fig. 9, Fig. S3, and Fig. S4 show the spread of the optimal solutions, plotted as red circles, with respect to the $RNGE$. Since the electricity cost is less expensive, one would expect that optimal solutions minimizing the cost are always associated with negative values of $RNGE$ close

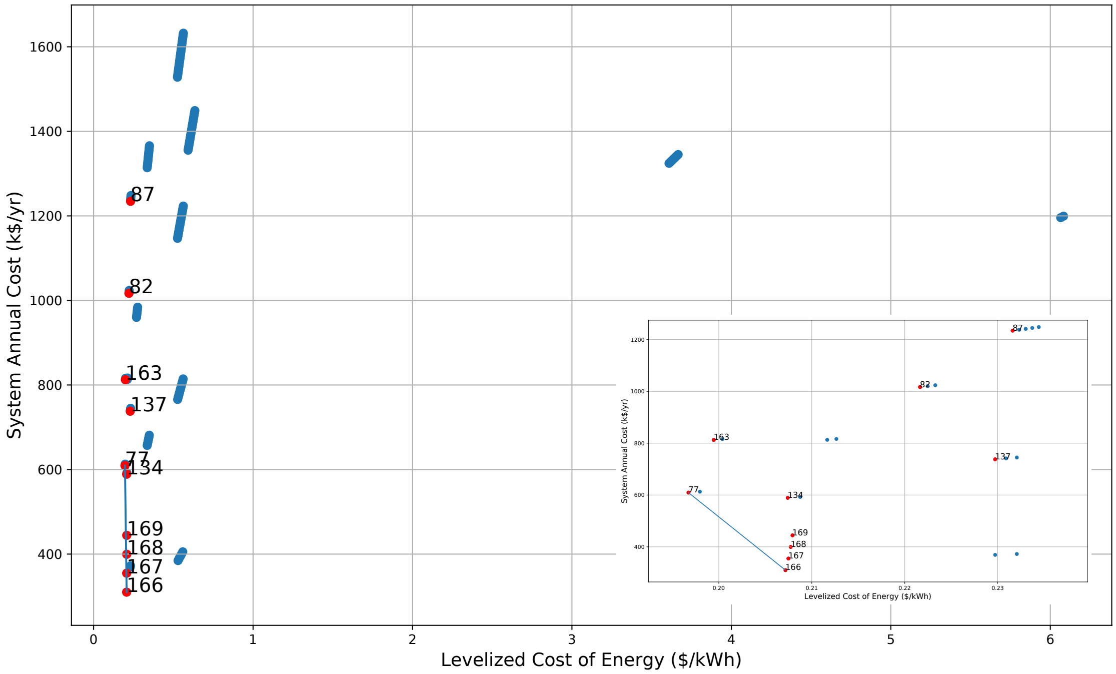

Fig. 8. Annual system cost and LCE for the configurations with a yearly net grid energy within ±5% relative to daily power consumption. The insert shows a closer look on the Pareto Front. The numbered points are the Pareto optimal set and are listed in Table 4.

to the cut-off value of −5%. However, Fig. 9 reveals the independency of the Pareto optimal set costs on the $RNGE$. That is, the optimal Pareto points are well spread over the $RNGE$ domain of ±5%. This assures the effectiveness of the analysis in finding the optimal system size.

The spread of the solution set can be attributed to the minimum constraint forced on the battery capacity, requiring it to power the electrolyzer for at least 12 continuous hours. This ensures that the system does not compensate the battery capacity and withdraws enormous amounts of energy from the grid to minimize the total cost. Another reason for the solution spread over the $RNGE$ domain of ±5% is the trade-off between the M_{pv} and Cap. To keep the system's cost at a minimal, a slight increase in M_{pv} must be accompanied by a slight decrease in Cap, which results in shifting the optimal point from a negative $RNGE$ value to a positive one.

3.3 Pareto Front Set as a Design Guide

Detailed examination of the Pareto Front set presented in Table 4 reveals the possibility of scaling the Pareto-Front according to any required plant capacity. To elaborate, if the required hydrogen production capacity of a plant is a double of any given point in the Pareto Front, it follows

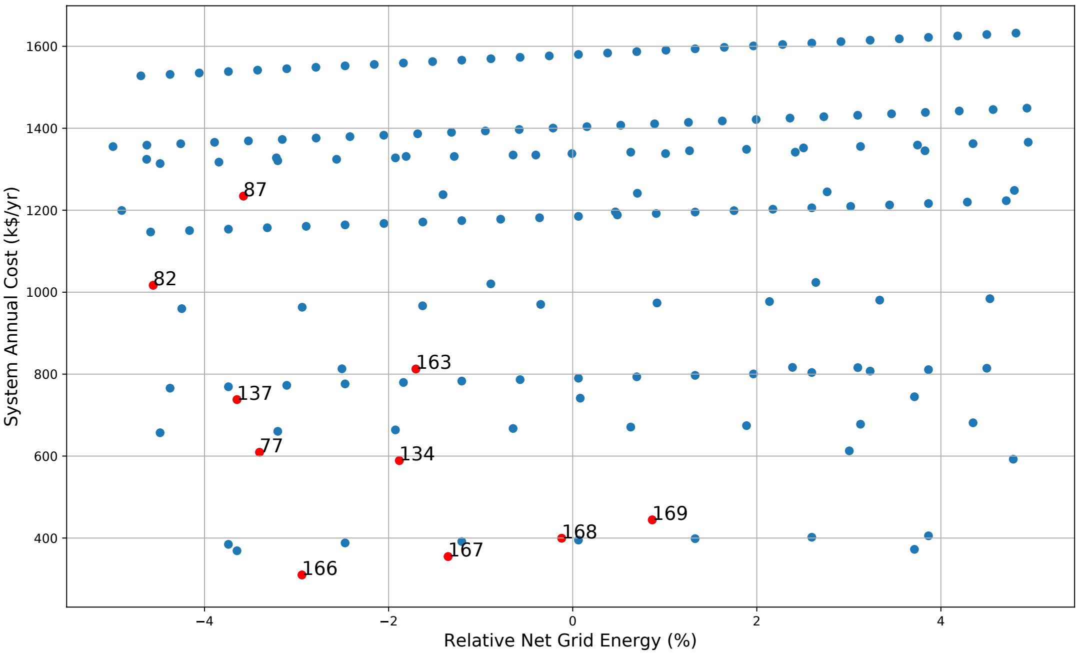

Fig. 9. Annual cost and the relative net grid energy, showing the 10 Pareto-Frontier points in red.

that M_{pv}, M, and Cap values are doubled as well to conserve the optimality of the solution. The new configuration will yield an optimal point with LCE and $RNGE$ values similar to the original Pareto point, and a doubled ACS value. This conclusion cannot be generalized to multiples of N (i.e. the value of N should be kept fixed), since the electrolysis cell current-voltage relation is nonlinear, and so would not result in an optimal design. Additionally, for safety requirements (mainly to prevent the current from reaching excessive values), the value of N must be specified based on the PV module output voltage.

To verify this conclusion, a new population is reproduced from each point in the original Pareto set in Table 4, using multipliers in the range 0.04 to 3.4. This range was specifically chosen to generate system sizing combinations with hydrogen production rates within the commercial scale of 5-120 Normal m^3/h. Due to the nature of this problem, only integer values of the newly generated design variables are accepted.

Fig. 10 shows the result of simulating the newly generated population. It should be noted that all points considered are proved to be optimal and constitute a refined version of the Pareto Front. It can be noticed from Fig. 10 that some points in the original Pareto, such as points 137, 82, and 87, were slightly dominated by newly generated designs. This is expected since, as previously mentioned in section 3.1, the step size of decision variables considered in the optimization problem limits the resulted Pareto-Front. To illustrate, point 137 in Table 4 was dominated by a newly generated design with similar N and M of 33 and 8, respectively, but with $Cap = 4120$ kWh and $M_{pv} = 5320$.

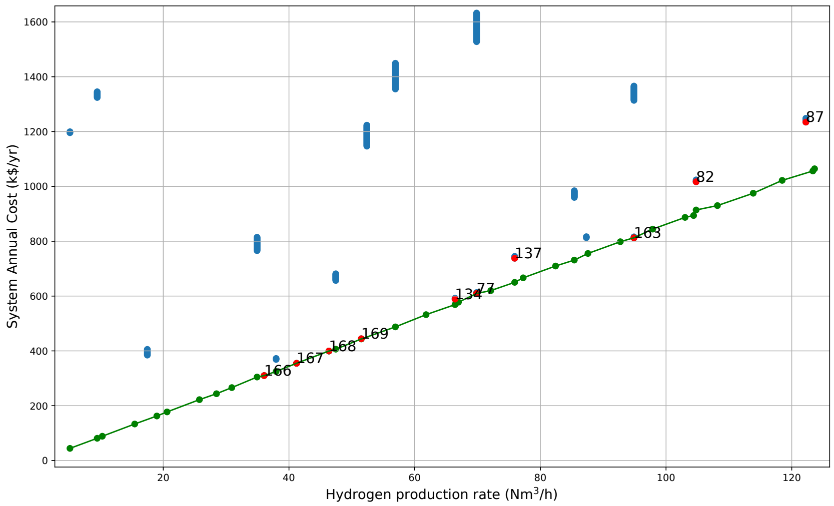

Fig. 10. Hydrogen production rate and the total annual system cost, showing the original 10 Pareto-Frontier points in red, and the refined Pareto Front in green. The numbered points are the original Pareto optimal set and are listed in Table 4.

It can be concluded from this case study, represented in Fig. 10, that the resulted set is guaranteed to be within the Pareto, and perform similar, if not better, than the original design it was re-produced from. This conclusion is significant because it enables the design of arbitrary plant capacities by multiplying a Pareto optimal point by a factor, while guaranteeing the new point still lies within the Pareto Front.

Typically, a plant design process begins by specifying a target hydrogen production capacity followed by a detailed economic and technical analysis. Hence, Table 4 can be used as a design guide, since it provides a range of possible plant capacities and the associated optimal size.

3.4 Sensitivity Analysis

In the following, the effect of each decision variable on the ACS, $V_{\mathrm{H_2}}$, LCE, and $RNGE$ is discussed, while keeping other variables fixed.

3.4.1 Battery Capacity

Obviously, increasing the battery capacity for a fixed system's size will increase the ACS. The LCE will increase as well because increasing the capacity only increases the numerator in Equation (38). However, $V_{\mathrm{H_2}}$ will not be influenced as it only depends on the electrolyzer design variables N, M.

The influence of battery capacity on the $RNGE$ depends on the system design elements that remain fixed. That is, the influence mainly depends on the system energy requirements and energy supplied by the PV modules. To illustrate, if the energy generated by PV modules is insufficient (relatively low M_{pv} values), then the $RNGE$ increases as Cap increases, as seen in Fig. S5(a) and Fig. S5(b). This is because higher Cap values will be associated with higher initial battery energy at the start of the simulation (since SOC_i=50%). Hence, less energy will be supplied by the grid throughout the year, causing the $RNGE$ to reach higher values. This also is confirmed by the fact that designs with higher Cap maintain higher SOC values throughout the year, requiring less grid energy.

For fixed sizes with relatively high energy production, the $RNGE$ behavior will be different, as shown in Fig. S5(c) and Fig. S5(d). As the Cap increases, the initial battery energy increases, and the SOC will be maintained at higher values throughout the simulation. Hence, the system will tend to sell energy to the grid rather than to acquire. The $RNGE$ behavior will then reach a maximum before it starts decreasing. As the Cap excessively increases, it will be more challenging to fully charge the battery, and less energy will be sold, as energy is only sold to the grid when the battery is fully charged.

In addition, as the battery capacity increases, both SLF and UF increase before reaching a plateau, which is expected as the numerator in Equations (44) and (45) increases. On the contrary, the $GEIF$ decreases as Cap increases, since having higher storage capacities will reduce the interaction with the grid. If the battery capacity further increases, it will no longer limit the system's performance and the performance will depend on the other design variables.

3.4.2 Number of PV modules

For a fixed size, the LCE will decrease exponentially as M_{pv} increases. This can be supported by examining Equation (38), where both $C_{\mathrm{a,pv}}$ and E_{an} increase linearly with increasing M_{pv}. The

$RNGE$ will increase as a result of increasing M_{pv}, as more energy will be produced, and hence, for a fixed system size, more energy will be sold to the grid and less energy is purchased from the grid. Similar to Cap, M_{pv} does not affect the hydrogen production rate, as it is assumed to be solely dependent on the electrolyzer design.

For the system annualized cost, Fig. S6 shows an increasing trend of the cost with increasing M_{pv}, hitting a minimum at lower M_{pv} values. At small M_{pv} values, the system is incapable of generating sufficient power for the electrolyzer, and an enormous amount of energy must be supplied by the grid, causing high total system cost. As M_{pv} slightly increases, the ability to meet the system's energy requirements increases. At this point, the increase in the PV system cost is less than the decrease in the cost of electricity supplied by the grid, leading to a reduced overall system cost. The curve reaches a minimum before the additional PV cost added to the system off-sets the savings in electricity costs, and as a result, the total cost starts rising. This behavior is independent of the system design kept fixed (i.e., similar behavior is noticed for all fixed values of N, M, and Cap).

With the increase in M_{pv} value, an exponential increase in SLF is noticed. The UF will experience an increase, before reaching a maximum, followed by a decrease in its value. Looking at Equation (45), as M_{pv} increases, both $E_{pv,tl}$ and E_{an} increase, with an overall increasing trend in UF value. It will reach a maximum before the increase in E_{an} exceeds the increase in $E_{pv,tl}$, reducing the overall value of UF. The behavior is reversed for the $GEIF$. Adding more PV modules to the system will increase the energy stored in the battery, which will reduce the amount of energy purchased from the grid, causing a reduction in $GEIF$. As M_{pv} further increases, the battery SOC will be maintained at high values and more energy will be sold to the grid, which will eventually cause $GEIF$ to increase.

3.4.3 Electrolyzer Cells and Stacks

Looking at Equation (38), the electrolyzer design variables N and M have no direct influence on the LCE. However, this conclusion is for a fixed system size, and should not be confused by the relation between V_{H_2} and LCE in Fig. 7, where the entire system size combination is different for each point in the plot.

As the number of stacks M increases, both V_{H_2} and ACS increase linearly. Nevertheless, the

$RNGE$ decreases exponentially. This exponential decrease is due to the linear increase in both NGE and P_e in Equation (40).

For an increasing number of cells N, the behavior is reversed. Increasing N will reduce V_{cell}, and consequently, I_{cell} will reduce according to Fig. 4. P_e and V_{H_2} will be more influenced by the decrease in I_{cell} and V_{cell}, rather than the slight increase in N values (from N=32 to 33 or 34). As less P_e is needed for higher N values, the $RNGE$ will increase and ACS will decrease.

3.5 Performance of Optimal Design

For each point in the Pareto Front, its performance throughout the year can be investigated. Point 77 in Table 4 is taken as an example in this section. Fig. 11 combines the net-grid energy and the coupled system operating conditions (P_e, P_{pv}, and E_b) as a function of time for two weeks of the year: the first week of January, Fig. 11(a), and the last week in July, Fig. 11(b). To get a visualization of the performance for the entire year, Fig. S7 provides the simulation results for the chosen optimal point (i.e. point 77 in Table 4).

Examining Fig. 11 reveals that the battery charges in cases where the PV power is in excess and discharges when PV power is insufficient to operate the electrolyzer. Additionally, energy is sold to the grid at fully charged states (with a noticeable increase in the net-grid energy curve) and is acquired from the grid when the battery reaches its DoD (associated with a decrease in the net-grid energy curve). Interestingly, the net-grid energy is following a decreasing-trend in the first week of January, Fig. 11(a), compared to the first week of August, Fig. 11(a), where it increases due to selling excess PV power produced. This is also reflected in Fig. S7, where the net-grid energy is decreasing at the beginning of the year (winter season), then slightly increases (between the AST hours of 1500 to 4000, corresponding to the spring season), followed by a sharp increase in the summer season months, and another decrease (corresponding to the fall and winter seasons) to meet a net-zero energy target at the end of the year. This proves that simulating the coupled system for an extended period of time, e.g. one year, reveals important information and enables enhanced system sizing that can respond to the plant requirements even during seasonal weather variations.

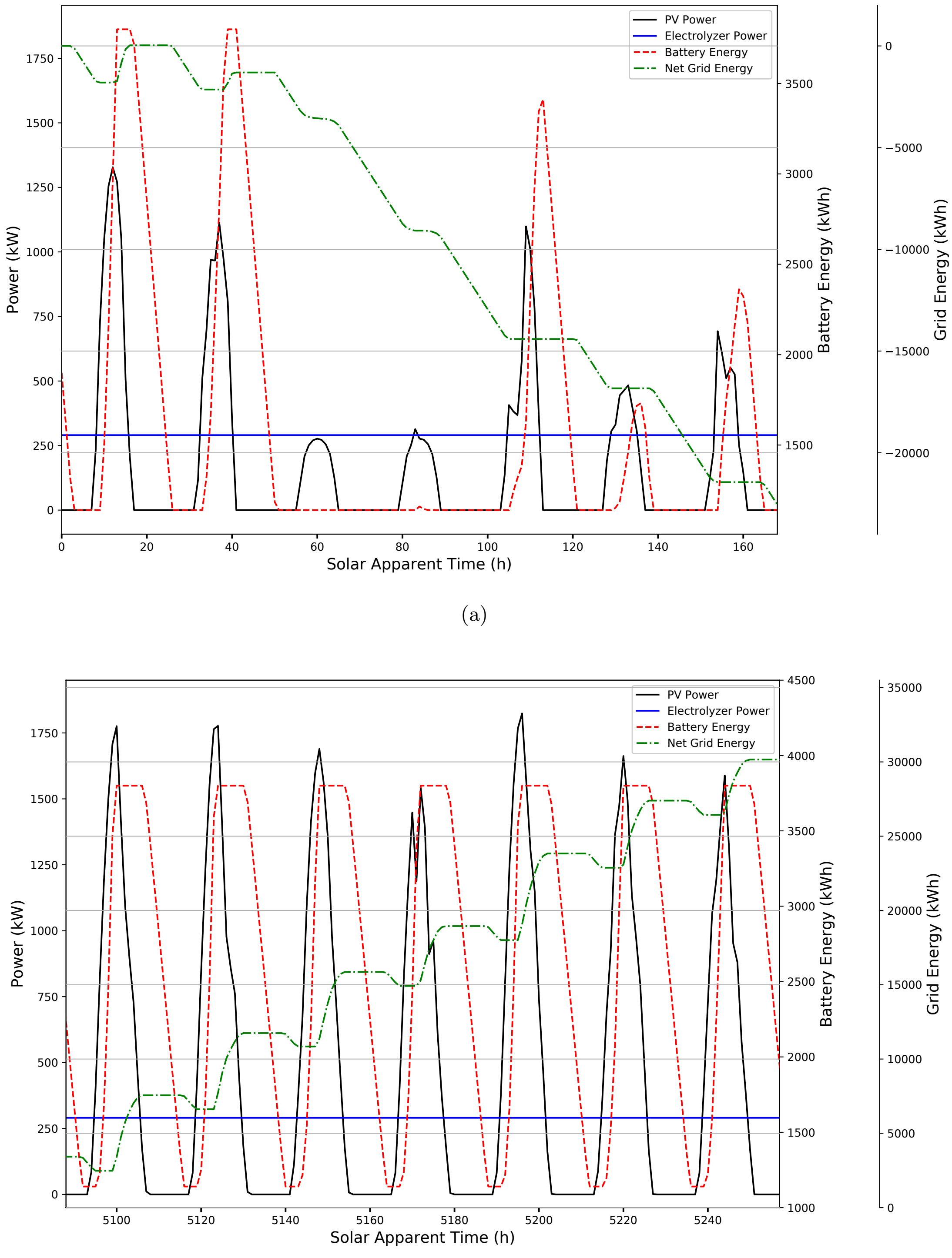

(a)

(b)

Fig. 11. Simulation results for point 77 in Table 4 for the first week of January (a), and the first week of August (b).

4 Conclusions

In this work, a coupled PV-electrolysis-battery system was studied with the goal of determining optimal system size, by implementing a Pareto Front analysis approach. This work presents a mathematical model to calculate the global irradiance falling on a PV module surface given its orientation, location, and time of the day. The model takes into account the diurnal and seasonal weather variations in College Park, MD for the calendar year 2017. The primary aim of the analysis was to identify the system design characteristics (N, M, M_{pv}, and Cap) that maximizes hydrogen production rate, minimizes the system's annualized cost and the levelized cost of energy, while maintaining an annual net grid energy within $\pm5\%$ relative to daily electrolyzer power consumption.

The simulation results yielded 170 sizing combinations with a $RNGE$ within $\pm5\%$, 10 of which were identified as the Pareto Front for this optimization problem. The identified Pareto Front can be used as a design guide, allowing the design of arbitrary plant capacity by scaling a Pareto optimal point, while guaranteeing the new point is optimal as well. The optimal Pareto set demonstrated STH values in the range 7-7.5%, SLF within 0.688-0.775, UF within 0.617-0.698, $GEIF$ within 0.418-0.595, and LCE values close to 0.2 \$/kWh, with hydrogen production capacities between 36-122 Nm^3/h. The influence of the design variables on the objective functions and performance indicators was investigated and is presented in this work. To support off-grid operations, it is recommended to maximize the SLF and UF, while minimizing the $GEIF$. This can be achieved by increasing the storage capacity of the battery to support the stand-alone operation of the system, which will highly reduce the dependency of the system on the grid, but will unfortunately increase the overall cost of the system. These performance indicators can also be enhanced with the incorporation and optimization of different renewable energy sources, such as wind or biomass. For future work, the effect of the design variables on the performance indicators (SLF, UF, and $GEIF$) will be included in the sizing optimization problem. It should be noted that the presented model can be further enhanced by including the effect of systems components degradation over the lifetime of the project.

The computational platform presented in this work to model integrated solar hydrogen systems can be extended to more complex hybrid systems. For instance, the use of wind power as a renewable energy source can be added to this problem to promote further sustainability and drive the system to off-grid limits. Additionally, it would be beneficial to evaluate the influence of incorporating environmental measures in the optimization problem, such as minimizing CO_2 emissions, for both off-grid and grid-connected designs. Subsequently, this allows for the enhancement of the current economic model through the inclusion of the costs associated with mitigating CO_2 emissions.

Another possibility for future work is the inclusion of post-production stages in the simulation, such as hydrogen purification, storage, conditioning, and distribution to the end user, which offer a broader perspective and can be nicely integrated with the current study to form a hydrogen supply chain network design problem. This allows the opportunity to introduce other measures to assess in the model, such as reliability, environmental impact, and safety.

Conflicts of interest

There are no conflicts to declare.

Acknowledgments

The first author gratefully acknowledge the support received from Kuwait University in the form of a graduate research fellowship. RAA gratefully acknowledges the support of the U.S. National Science Foundation through Grant No. CBET1438375 and NASA through the Goddard Space Flight Center.

References

[1] Hosseini, S. E. and M. Abdul Wahid. "Hydrogen Production from Renewable and Sustainable Energy Resources: Promising Green Energy Carrier for Clean Development". *Renewable & Sustainable Energy Reviews* **57** (2016) 850-866. DOI: 10.1016/j.rser.2015.12.112

[2] Staffell, I., D. Scamman, A. V. Abad, P. Balcombe, P. E. Dodds, P. Ekins, N. Shah and K. R. Ward. "The role of hydrogen and fuel cells in the global energy system". *Energy & Environmental Science* **12** 2 (2019) 463-491. DOI:10.1039/C8EE01157E

[3] Brandon, N. P. and Z. Kurban. "Clean energy and the hydrogen economy". *Philosophical Transactions of the Royal Society A* **375** 2098 (2017). DOI: 10.1098/rsta.2016.0400

[4] Ursua, A., L. M. Gandia, and P. Sanchis. "Hydrogen production from water electrolysis: current status and future trends". *Proceedings of the IEEE* **100** 2 (2012). DOI:10.1109/JPROC.2011.2156750

[5] Atilhan, S., Park, S., El-Halwagi, M. M., Atilhan, M., Moore, M., and Nielsen, R. B. Green hydrogen as an alternative fuel for the shipping industry. *Current Opinion in Chemical Engineering* **31** (2021) 100668. DOI: 10.1016/j.coche.2020.100668

[6] Abad, A. V., and Dodds, P. E. Green hydrogen characterisation initiatives: Definitions, standards, guarantees of origin, and challenges. *Energy Policy* **138** (2020) 111300. DOI: 10.1016/j.enpol.2020.111300

[7] Gardner, D.. "Hydrogen production from renewables". *Renewable Energy Focus* **9** 7 (2009) 34-37. DOI: 10.1016/S1755-0084(09)70036-5

[8] Santos, D. M., C. A. Sequeira, and J. L. Figueiredo. "Hydrogen production by alkaline water electrolysis". *Quimica Nova* **36** 8 (2013) 1176-1193. DOI: 10.1590/S0100-40422013000800017

[9] Gibson, T. L. and N. A. Kelly. "Optimization of solar powered hydrogen production using photovoltaic electrolysis devices". *International Journal of Hydrogen Energy* **33** 21 (2008) 5931-5940. DOI:10.1016/j.ijhydene.2008.05.106

[10] Dahbi, S., R. Aboutni, A. Aziz, N. Benazzi, M. Elhafyani, and K. Kassmi. "Optimised hydrogen production by a photovoltaic-electrolysis system dc/dc converter and water flow controller". *International Journal of Hydrogen Energy* **41** 45 (2016) 20858-20866. DOI:10.1016/j.ijhydene.2016.05.111

[11] Cabezas, M. D., J. I. Franco, and H. J. Fasoli. "Optimization of self-regulated hydrogen production from photovoltaic energy". *International Journal of Hydrogen Energy* **45** 17 (2020) 10391-10397. DOI:10.1016/j.ijhydene.2018.10.203

[12] Sriramagiri, G. M., Luc, W., Jiao, F., Ayers, K., Dobson, K. D., and Hegedus, S. S. "Computation and assessment of solar electrolyzer field performance: Comparing coupling strategies". *Sustainable Energy & Fuels* **3** 2 (2019) 422–430. DOI: 10.1039/c8se00399h

[13] Khalilnejad, A., A. Sundararajan, and A. I. Sarwat. ”Optimal design of hybrid wind/photovoltaic electrolyzer for maximum hydrogen production using imperialist competitive algorithm”. *Journal of Modern Power Systems and Clean Energy* **6** 1 (2018) 40-49. DOI:10.1007/s40565-017-0293-0

[14] Conibeer, G. J. and B. S. Richards. ”A comparison of PV/electrolyser and photoelectrolytic technologies for use in solar to hydrogen energy storage systems”. *International Journal of Hydrogen Energy* **32** (2007) 2703-2711. DOI:10.1016/j.ijhydene.2006.09.012

[15] Lagorse, J., D. Paire, and A. Miraoui. ”Sizing optimization of a stand-alone street lighting system powered by a hybrid system using fuel cell, PV and battery”. *Renewable Energy* **34** 3 (2009) 683-691. DOI:10.1016/j.renene.2008.05.030

[16] Hassan, S. Z., S. Mumtaz, T. Kamal, and L. Khan. ”Performance of grid-integrated photovoltaic/fuel cell/electrolyzer/battery hybrid power system”. *Power Generation System and Renewable Energy Technologies (PGSRET)* 1-8 IEEE (2015). DOI:10.1109/PGSRET.2015.7312249

[17] Singh S., P. Chauhan, and N. Singh. ”Capacity optimization of grid connected solar/fuel cell energy system using hybrid ABC-PSO algorithm”.*International Journal of Hydrogen Energy* **45** 16 (2020) 10070–10088. DOI:10.1016/j.ijhydene.2020.02.018

[18] Gabriel Rullo, P., R. Costa-Castello, V. Roda, and D. Feroldi. ”Energy management strategy for a bioethanol isolated hybrid system: simulations and experiments”. *Energies* **11** 6 (2018) 1362-1362. DOI:10.3390/en11061362

[19] Ozgirgin, E., Y. Devrim, and A. Albostan. ”Modeling and simulation of a hybrid photovoltaic (PV) module-electrolyzer-PEM fuel cell system for micro-cogeneration applications”. *International Journal of Hydrogen Energy* **40** 44 (2015) 15336-15342. DOI: 10.1016/j.ijhydene.2015.06.122

[20] Ghenai C., T. Salameh, and A. Merabet. ”Technico-economic analysis of off grid solar PV/fuel cell energy system for residential community in desert region”. *International Journal of Hydrogen Energy* **45** 20 (2020) 11460–11470. DOI:10.1016/j.ijhydene.2018.05.110

[21] Tebibel H., A. Khellaf, S. Menia, and I. Nouicer. ”Design, modelling and optimal power and hydrogen management strategy of an off grid PV system for hydrogen production using methanol electrolysis”. *International Journal of Hydrogen Energy* **42** 22 (2017) 14950–14967. DOI:10.1016/j.ijhydene.2017.05.010

[22] Cabezas, M. D., E. A. Wolfram, J. I. Franco, and J. Fasoli Hector. ”Hydrogen vector for using PV energy obtained at Esperanza base, Antarctica”. *International Journal of Hydrogen Energy* **42** 37 (2017) 23455-23463. DOI:10.1016/j.ijhydene.2017.02.188

[23] Yang, H., Z. Wei, and L. Chengzhi. ”Optimal design and techno-economic analysis of a hybrid solar-wind power generation system”. *Applied Energy* **86** 2 (2009) 163-169. DOI:10.1016/j.apenergy.2008.03.008

[24] Baghaee H. R., M. Mirsalim, G. B. Gharehpetian, and H. A.Talebi. ”Reliability/cost-based multi-objective pareto optimal design of stand-alone wind/PV/FC generation microgrid system”. *Energy* **115** (2016) 1022–1041. DOI:10.1016/j.energy.2016.09.007

[25] Hosseinalizadeh R., G. H. Shakouri, M. S. Amalnick, and P. Taghipour. ”Economic sizing of a hybrid (PV-WT-FC) renewable energy system (HRES) for stand-alone usages by an optimization-simulation model: case study of Iran”. *Renewable and Sustainable Energy Reviews.* **54** (2016) 139–150. DOI:10.1016/j.rser.2015.09.046

[26] Mukherjee U., A. Maroufmashat, J. Ranisau, M. Barbouti, A. Trainor, N. Juthani, H. El-Shayeb, and M. Fowler. ”Techno-economic, environmental, and safety assessment of hydrogen powered community microgrids; case study in Canada”. *International Journal of Hydrogen Energy* **42** 20 (2017) 14333–14349. DOI:10.1016/j.ijhydene.2017.03.083

[27] Adomaitis, R. A.. *Solar energy lecture notes: ”Modeling and analysis of photovoltaic and related solar energy systems”* (2018) 16–30.

[28] Wenham, S. R., M. A. Green, M. E. Watt, R. Corkish, and A. Sprou. *Applied Photovoltaics.* 3rd ed. Hoboken: Taylor and Francis (2011) 18–19. DOI:10.4324/9781849776981

[29] Badescu, Viorel. ”Verification of Some Very Simple Clear and Cloudy Sky Models to Evaluate Global Solar Irradiance”. *Solar Energy* **61**(4) (1997), 251-264.

[30] The Dark Sky API. https://darksky.net. Accessed June 6, 2018.

[31] Gansler, R. A., S. A. Klein, and W. A. Beckman. "Investigation of minute solar radiation data". *Solar Energy* **55** 1 (1995) 21-27. DOI:10.1016/0038-092X(95)00025-M

[32] Li, Y., X. M. Chen, B. Y. Zhao, Z. G. Zhao, and R. Z. Wang. "Development of a PV performance model for power output simulation at minutely resolution". *Renewable Energy* **111** (2017) 732-739. DOI:10.1016/j.renene.2017.04.049

[33] SunPower product data sheet. Retrieved from: https://us.sunpower.com/solar-panels-technology/x-series-solar-panels/. Accessed May 17, 2018.

[34] Ulleberg, O.. "Modeling of advanced alkaline electrolyzers: a system simulation approach". *International Journal of Hydrogen Energy* **28** 1 (2003) 21-33. DOI:10.1016/S0360-3199(02)00033-2

[35] Zeng, K. and D. Zhang. "Recent progress in alkaline water electrolysis for hydrogen production and applications". *Progress in Energy and Combustion Science* **36** 3 (2010) 307-326. DOI:10.1016/j.pecs.2009.11.002

[36] Esposito, D. V.. "Membraneless electrolyzers for low-cost hydrogen production in a renewable energy future". *Joule* **1** 4 (2017) 651-658. DOI:10.1016/j.joule.2017.07.003

[37] AGFA Specialty Products. https://www.agfa.com/specialty-products/solutions/membranes/zirfon/. Accessed May 22, 2018.

[38] Alobaid, A., C. Wang, and R. A. Adomaitis. "Mechanism and Kinetics of HER and OER on NiFe LDH Films in an Alkaline Electrolyte". *Journal of the Electrochemical Society* **165** 15 (2018) J3395-J3404. DOI:10.1149/2.0481815jes

[39] Gilliam, R. J., J. W. Graydon, D. W. Kirk, and S. J. Thorpe. "A review of specific conductivities of potassium hydroxide solutions for various concentrations and temperatures". *International Journal of Hydrogen Energy* **32** 3 (2007) 359-364. DOI:10.1016/j.ijhydene.2006.10.062

[40] May, G. J., A. Davidson, and B. Monahov. "Lead batteries for utility energy storage: a review". *Journal of Energy Storage* **15** (2018) 145-157. DOI:10.1016/j.est.2017.11.008

[41] Fathima, H. and K. Palanisamy. "Optimized sizing, selection, and economic analysis of battery energy storage for grid-connected wind-PV hybrid system". *Modelling and Simulation in Engineering* **2015** (2015). DOI:10.1155/2015/713530

[42] Fu, R., D. Feldman, R. Margolis, M. Woodhouse, and K. Ardani. "U.S. solar photovoltaic system cost benchmark: Q1 2017". *National Renewable Energy Laboratory* (2017). Retrieved from: https://www.nrel.gov/docs/fy17osti/68925.pdf. Accessed December 7, 2018.

[43] Buttler, A. and H. Spliethoff. "Current status of water electrolysis for energy storage, grid balancing and sector coupling via power-to-gas and power-to-liquids: a review". *Renewable and Sustainable Energy Reviews* **82** (2018) 2440-2454. DOI:10.1016/j.rser.2017.09.003

[44] Locatelli, G., S. Boarin, A. Fiordaliso, and M. Ricotti. "Load following of small modular reactors (smr) by cogeneration of hydrogen: A techno-economic analysis". *Energy* **148** (2018). DOI:10.1016/j.energy.2018.01.041

[45] Bertuccioli, L., A. Chan, D. Hart, F. Lehner, B. Madden, and E. Standen. "Development of water electrolysis in the European Union". *Fuel Cells and Hydrogen Joint Undertaking* (2014). Retrieved from: https://www.fch.europa.eu/node/783. Accessed December 27, 2018.

[46] Dufo-Lopez, R., J. M. Lujano-Rojas, and J. L. Bernal-Agustin. "Comparison of different lead-acid battery lifetime prediction models for use in simulation of stand-alone photovoltaic systems". *Applied Energy* **115** (2014) 242-253. DOI:10.1016/j.apenergy.2013.11.021

[47] The U.S. Energy Information Administration, "2017 average monthly bill- commercial". Retrieved from: https://www.eia.gov/electricity/sales_revenue_price/pdf/table5_b.pdf. Accessed December 27, 2018.

[48] Yang, H., L. Lu, and W. Zhou. "A novel optimization sizing model for hybrid solar-wind power generation system". *Solar Energy* **81** 1 (2007) 76-84. DOI:10.1016/j.solener.2006.06.010

[49] Hernandez, C., Y. Naranjani, Y. Sardahi, W. Liang, O. Schutze, and J. Sun. "Simple cell mapping method for multi-objective optimal feedback control design". *International Journal of Dynamics and Control* **1** 3 (2013) 231-238. DOI:10.1007/s40435-013-0021-1

[50] Herdem, M. S., Mazzeo, D., Matera, N., Wen, J. Z., Nathwani, J., and Hong, Z. ”Simulation and modeling of a combined biomass gasification-solar photovoltaic hydrogen production system for methanol synthesis via carbon dioxide hydrogenation”. *Energy Conversion and Management* (2020), **219**, 113045.

[51] Mazzeo, D., Herdem, M. S., Matera, N., and Wen, J. Z. ”Green hydrogen production: Analysis for different single or combined large-scale photovoltaic and wind renewable systems”. *Renewable Energy* (2022) **200**, 360–378.